

The Impact of Non-Gaussian Errors on Weak Lensing Surveys

Masahiro Takada^{1*} and Bhuvnesh Jain^{2†}

¹*Institute for the Physics of Mathematics of the Universe (IPMU), The University of Tokyo, Chiba 277-8582, Japan*

²*Department of Physics and Astronomy, University of Pennsylvania, Philadelphia, PA 19104, USA*

24 October 2008

ABSTRACT

The weak lensing power spectrum carries cosmological information via its dependence on the growth of structure and on geometric factors. Since much of the cosmological information comes from scales affected by nonlinear clustering, measurements of the lensing power spectrum can be degraded by non-Gaussian covariances. Recently there have been conflicting studies about the level of this degradation. We use the halo model to estimate it and include new contributions related to the finite size of lensing surveys, following Rimes and Hamilton’s study of 3D simulations. We find that non-Gaussian correlations between different multipoles can degrade the cumulative signal-to-noise for the power spectrum amplitude by up to a factor of 2 (or 5 for a worst-case model that exceeds current N-body simulation predictions). However, using an eight-parameter Fisher analysis we find that the marginalized errors on individual parameters are degraded by less than 10% (or 20% for the worst-case model). The smaller degradation in parameter accuracy is primarily because: individual parameters in a high-dimensional parameter space are degraded much less than the volume of the full Fisher ellipsoid; lensing involves projections along the line of sight, which reduce the non-Gaussian effect; some of the cosmological information comes from geometric factors which are not degraded at all. We contrast our findings with those of Lee & Pen (2008) who suggested a much larger degradation in information content. Finally, our results give a useful guide for exploring survey design by giving the cosmological information returns for varying survey area, depth and the level of some systematic errors.

Key words: cosmology: theory — gravitational lensing — large-scale structure of universe

1 INTRODUCTION

Over the last decade a concordance model has emerged in cosmology in which about two-thirds of the energy density of the universe today may be in the form of dark energy. This explains the observation that we reside in an accelerating universe (Riess et al. 1998; Perlmutter et al. 1999). Despite its importance to the formation and evolution of the universe there are no compelling theories that explain the energy density or the properties of dark energy.

To address questions about the nature of dark energy a number of ambitious wide-field optical and infrared imaging surveys have been proposed. These range from space-based missions in the optical and infrared, such as the Supernova Acceleration Probe (SNAP¹, proposed as the space-based Joint Dark Energy Mission (JDEM)), and the Dark Energy UNiverse Explore (DUNE²), to ground-based surveys such as the Panoramic Survey Telescope & Rapid Response System (Pan-STARRS³), the Dark Energy Survey (DES⁴), the Subaru Weak Lensing Survey (Miyazaki et al. 2006), the Large Synoptic Sky Survey (LSST⁵) and others. Each of these missions approaches the study of dark energy using multiple, complementary observational probes: gravitational weak lensing (WL) to study the growth of structure and geometry, baryon oscillations to measure the angular diameter distance vs. redshift relation, and Type Ia supernovae to measure the luminosity distance vs. redshift relation.

In this paper we focus on one of these probes, weak lensing or the so-called cosmic shear, the bending of light by intervening mass

* E-mail: masahiro.takada@ipmu.jp

† E-mail: bjain@physics.upenn.edu

¹ <http://www.snap.lbl.gov>

² <http://www.dune-mission.net/>

³ <http://pan-starrs.ifa.hawaii.edu>

⁴ <http://www.darkenergysurvey.org>

⁵ <http://www.lsst.org>

distribution that causes images of distant galaxies to be distorted (e.g. Bartelmann & Schneider 2001 for a thorough review). These sheared source galaxies are mostly too weakly distorted for us to measure the effect on single galaxies, but require large surveys containing millions of galaxies to detect the signal in a statistical way. The conventional method used for measuring cosmic shear is the two-point correlation function whose Fourier-transform is the shear power spectrum. Cosmic shear correlations have been observed by various groups and used to constrain cosmological parameters (most recently by Fu et al. 2008 using the Canada-France-Hawaii Telescope Legacy Survey (CFHTLS)).

Lensing tomography refers to the use of depth information in the source galaxies to get three-dimensional information about the lensing mass (Hu 1999; Huterer 2002; Heavens 2003; Takada & Jain 2004; Song & Knox 2004; Takada & White 2004; also see Hoekstra & Jain 2008 for a recent review). By binning source galaxies in photometric redshift bins, the evolution of the lensing power spectrum can be measured as a function of redshift and angular scale. This greatly improves the sensitivity of lensing to the geometry of the universe as well as the growth of mass clustering, both of which are sensitive to the nature of dark energy. This method has emerged as one of the most promising to obtain precise constraints on the nature of dark energy if the systematic errors are well under control (e.g., Albrecht et al. 2006).

Given the resources required for such surveys, it is important to understand the statistical precision of cosmic shear observables and error propagation in determination of cosmological parameters. Since cosmic shear probes the projected mass distribution, the statistical properties of the cosmic shear field reflect those of the mass distribution. For the case of the cosmic shear power spectrum, its statistical precision is determined by the covariance that contains three kinds of contributions: the shot noise contamination due to intrinsic ellipticities, and the Gaussian and non-Gaussian sample variances caused by the imperfect sampling of the fluctuations (Scoccimarro et al. 1999; Cooray & Hu 2001). The non-Gaussian sample variance arises from the projection of the mass trispectrum weighted with the lensing efficiency kernel. In fact most of the useful cosmological information contained in the lensing power spectrum lies on small angular scales that are affected by nonlinear clustering. Therefore non-Gaussian errors can be significant in weak lensing measurements as indicated by a few previous studies based on ray tracing simulations (White & Hu 2000; Semboloni et al. 2007) and the halo model approach (Cooray & Hu 2001). However, the importance of non-Gaussian errors is not yet fully understood, especially in terms of the prospects of future surveys for constraining dark energy. This will be also important in exploring optimal survey design for planned surveys.

Therefore, the aim of this paper is to study the covariances of the lensing power spectrum based on the halo model approach (Cooray & Sheth 2002 for a thorough review), and to estimate the impact of the non-Gaussian errors on the power spectrum measurement as well as on the determination of cosmological parameters. We also study how the effect of the non-Gaussian errors varies with survey parameters (depth and area) and in the presence of systematic errors – photometric redshift errors and shear calibration errors. Our analysis includes new sources of non-Gaussian errors that inevitably arise for a finite survey area, called the beat-coupling effect. This was pointed out by Rimes & Hamilton 2005 for the case of the 3D mass power spectrum (also see Hamilton et al. 2006; Sefussati et al. 2006; Neyrinck et al. 2006). More explicitly, if the scale of interest is embedded in a large-scale (of order the survey size) overdensity or underdensity, then the small scale fluctuations we want to measure may grow more rapidly or slowly than the ensemble average. This is predicted by perturbation theory for gravitational clustering. This physical correlations with the unseen large-scale fluctuations may add uncertainties in measuring the power spectrum at scales of interest.

Very recently, Lee & Pen (2008) claimed that, by studying the angular power spectrum of the SDSS galaxy distribution (i.e. not directly from lensing data), the effect of the non-Gaussian errors is very significant on angular scales of ~ 10 arcminutes: they found that the cumulative signal-to-noise ratio integrated over a range of multipoles is two orders of magnitude lower than the case of the Gaussian fluctuations. Since galaxies are related to the lensing mass fluctuations, does this imply that the non-Gaussian errors significantly degrade the ability of lensing surveys to constrain cosmology? This is the issue we would like to carefully address in this paper.

The structure of this paper is as follows. We define the lensing power spectrum in the context of lensing tomography in Section 2 and the lensing covariances including the beat-coupling effect in Section 3. In Section 4 we show the results for the impact of non-Gaussian covariances on the power spectrum measurement and parameter estimations. In Section 5 we study the covariances for the cosmic shear correlation functions. Section 6 is devoted to a discussion of our conclusions.

2 PRELIMINARIES

2.1 A Λ CDM Model

We will throughout this paper work in the context of a spatially flat cold dark matter model for structure formation. The expansion history of the universe is given by the scale factor $a(t)$ in a homogeneous and isotropic universe (e.g., see Dodelson 2003). The expansion rate, $H(t) \equiv \dot{a}(t)/a(t)$, is specified once the matter density Ω_{m0} (the cold dark matter plus the baryons) and dark energy density Ω_{de0} at present in units of the critical density $3H_0^2/(8\pi G)$ are given, where $H_0 = 100 h \text{ km s}^{-1} \text{ Mpc}^{-1}$ is the Hubble parameter at present:

$$H^2(a) = H_0^2 \left[\Omega_{m0} a^{-3} + \Omega_{de0} e^{-3 \int_1^a da' (1+w(a'))/a'} \right], \quad (1)$$

where we have employed the normalization $a(t_0) = 1$ today and $w(a)$ specifies the equation of state for dark energy as $w(a) \equiv p_{de}(a)/\rho_{de}(a)$. Note that $\Omega_{m0} + \Omega_{de0} = 1$ and $w = -1$ corresponds to a cosmological constant. The comoving distance $\chi(a)$ from an observer at $a = 1$ to a source at a is expressed in terms of the Hubble expansion rate as

$$\chi(a) = \int_a^1 \frac{da'}{H(a')a'^2}. \quad (2)$$

This gives the distance-redshift relation $\chi(z)$ via the relation $1 + z = 1/a$.

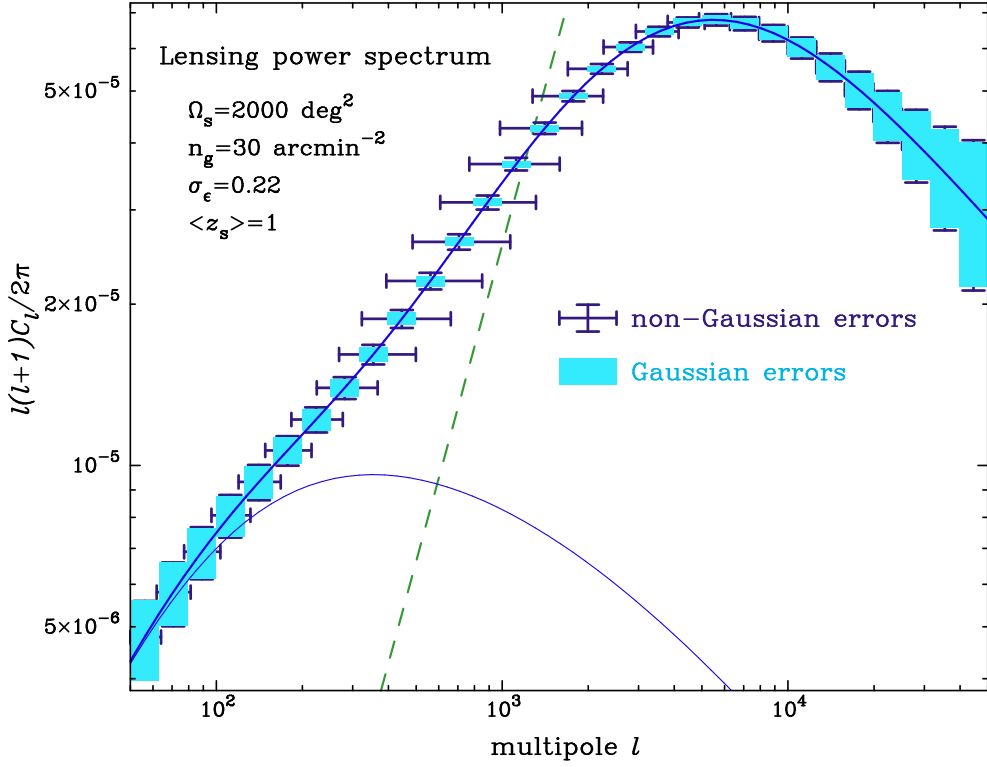


Figure 1. The lensing power spectrum expected from our fiducial 2000 deg^2 ground-based survey. The bold solid curve shows the prediction for the Λ CDM model (including non-linear evolution) while the thin solid curve denotes the linear theory prediction. The shaded boxes around the bold solid curve show the expected measurement errors at each multipole bin assuming Gaussian errors. The vertical and horizontal error bars around the bold solid curve show non-Gaussian effects. The horizontal error bars display correlations between neighboring multipole bins caused by the non-Gaussian errors, while the vertical error bars show the increase in errors compared to the Gaussian errors (shaded boxes).

Next we need the redshift growth of density perturbations. In linear theory after matter-radiation equality, all Fourier modes of the mass density perturbation, $\delta(\mathbf{x}) (\equiv \delta\rho_m(\mathbf{x})/\bar{\rho}_m)$, grow at the same rate, the growth rate (e.g. see Eqn. 10 in Takada 2006 for details). Note that throughout this paper we ignore effects of finite mass neutrinos and clustered dark energy on the growth rate, causing a scale-dependent growth rate (e.g., Saito et al. 2008; Takada 2006).

2.2 Tomographic Power Spectra of Cosmic Shear

Gravitational shear can be simply related to the lensing convergence: the weighted mass distribution integrated along the line of sight (e.g., see Mellier 1999; Bartelmann & Schneider 2001; Schneider 2006 for thorough reviews). Photometric redshift information on source galaxies allows us to subdivide galaxies into redshift bins, enabling more cosmological information to be extracted, which is referred to as lensing tomography (e.g., Hu 1999; Huterer 2002; Takada & Jain 2004). In the context of cosmological gravitational lensing the convergence field with tomographic information is expressed as a weighted projection of the three-dimensional mass density fluctuation field:

$$\kappa_{(i)}(\boldsymbol{\theta}) = \int_0^{\chi_H} d\chi W_{(i)}(\chi) \delta[\chi, \chi\boldsymbol{\theta}], \quad (3)$$

where $\boldsymbol{\theta}$ is the angular position on the sky, χ is the comoving angular diameter distance, and χ_H is the distance to the Hubble horizon. The lensing weight function $W_{(i)}(\chi)$ in the i -th redshift bin, defined to lie between the comoving distances χ_i and χ_{i+1} , is given by

$$W_{(i)}(\chi) = \begin{cases} \frac{W_0}{\bar{n}_i} a^{-1}(\chi) \chi \int_{\chi_i}^{\chi_{i+1}} d\chi_s n_s(z) \frac{dz}{d\chi_s} \frac{\chi_s - \chi}{\chi_s}, & \chi \leq \chi_{i+1}, \\ 0, & \chi > \chi_{i+1}, \end{cases} \quad (4)$$

where $W_0 \equiv (3/2) \Omega_{m0} H_0^2$ and $n_s(z)$ is the redshift selection function of source galaxies, which is normalized as $\int_0^\infty dz n_s(z) = \bar{n}_g$ with \bar{n}_g being the average number density of galaxies per unit steradian (see around Eqn. [20] in § 4.1 for our definition of the source redshift distribution). Also \bar{n}_i is the average number density of sub-sample galaxies in the i -th redshift bin defined as

$$\bar{n}_i = \int_{\chi_i}^{\chi_{i+1}} d\chi_s n_s(z) \frac{dz}{d\chi_s}. \quad (5)$$

The cosmic shear fields are measurable only in a statistical sense. The most conventional methods used in the literature are the shear two-point correlation function. The Fourier transformed counterpart is the shear power spectrum. For lensing tomography of n_z redshift bins, using the flat-sky and Limber's approximations (Limber 1954), there are $n_z(n_z + 1)/2$ spectra available:

$$P_{(ij)}(l) = \int_0^{\chi_H} d\chi W_{(i)}(\chi) W_{(j)}(\chi) \chi^{-2} P_\delta \left(k = \frac{l}{\chi}; \chi \right), \quad (6)$$

where $P_\delta(k)$ is the three-dimensional mass power spectrum. Note that hereafter the quantities with subscript “ δ ” denote those of the mass density fluctuations. For $l \gtrsim 100$ the major contribution to $P_{(ij)}(l)$ comes from non-linear clustering (e.g., see Fig. 2 in Takada & Jain 2004). We employ the fitting formula for the non-linear $P_\delta(k)$ proposed in Smith et al. (2003), assuming that it can be applied to dark energy cosmologies by replacing the growth rate used in the formula with that for a given dark energy model. We note in passing that the issue of accurate power spectra for general dark energy cosmologies still needs to be addressed carefully (Huterer & Takada 2005; also see Ma 2007 for the related discussion).

As can be found from Eqn. (6), the lensing power spectra contain cosmological information via both the lensing efficiency kernel and the mass clustering information contained in P_δ , e.g. which almost equally contribute to the final sensitivity to dark energy parameters. On the other hand, the non-Gaussian errors of the lensing fields arise from the non-Gaussianity of the nonlinear mass clustering in structure formation. Thus, even if the underlying mass distribution is highly non-Gaussian, the cosmological information the lensing carries would be to some extent preserved via the lensing efficiency kernel, which is one of notable differences from other methods such as the galaxy power spectrum.

In reality, the observed power spectrum is contaminated by the intrinsic ellipticity noise. Assuming that the intrinsic ellipticity distribution is uncorrelated between different galaxies, the observed power spectrum between redshift bins i and j can be expressed as

$$P_{(ij)}^{\text{obs}}(l) = P_{(ij)}(l) + \delta_{ij}^K \frac{\sigma_\epsilon^2}{\bar{n}_{(i)}} \quad (7)$$

where σ_ϵ is the rms intrinsic ellipticities per component. Note that the shot noise contamination could be positive and negative due to the statistical nature of shear, in contrast to the galaxy power spectrum where the shot noise contamination is always positive definite due to the nature of point statistics. It should be also noted that the Kronecker delta symbol δ_{ij}^K accounts for the fact that the cross-spectra with $i \neq j$ are not contaminated by the shot noise. Therefore the shot noise contamination needs not be subtracted from the estimated cross spectra that would reduce residual uncertainties in practice.

3 COVARIANCES OF THE COSMIC SHEAR POWER SPECTRA

3.1 Definition

In reality the lensing power spectrum has to be estimated from the Fourier or spherical harmonic coefficients of the observed lensing fields constructed for a finite survey. In this paper we assume the flat-sky approximation and thus use Fourier wavenumbers l , which are equivalent to spherical harmonic multipoles l in the limit $l \gg 1$ (Hu 2000). Because the survey is finite, an infinite number of Fourier modes are not available, and rather the discrete Fourier decomposition has to be constructed in terms of the fundamental mode that is limited by the survey size as will be in detail discussed below. We assume a homogeneous survey geometry for simplicity and do not consider any complex boundary and/or masking effects. For this case, as shown in Appendix B of Takada & Bridle (2007), the lensing power spectrum of the a -th multipole bin, l_a , may be estimated as

$$P_{(ij)}^{\text{est}}(l_a) = \frac{1}{\Omega_s} \int_{|l'| \in l_a} \frac{d^2 l'}{A(l_a)} \tilde{\kappa}_{(i)} l' \tilde{\kappa}_{(j)} - l', \quad (8)$$

where Ω_s is the survey area, the integration range is confined to the Fourier modes lying in the annulus of a given width, $l_a - \Delta l_a/2 \leq l' \leq l_a + \Delta l_a/2$ and $A(l_a)$ denotes the integration area in the Fourier space approximately given by $A(l_a) \equiv \int_{|l'| \in l_a} d^2 l' \approx 2\pi l_a \Delta l_a$ for the case of $l_a \gg \Delta l_a$. Throughout this paper we use the subscripts a, b to denote the multipole bins, while we use the subscripts i, j or i', j' to denote the redshift bins.

Once an estimator of the lensing power spectrum is defined, it is straightforward to compute the covariance (Scoccimarro et al 1999; Cooray & Hu 2001; Takada & Bridle 2007). The covariance of cosmic shear power spectra describes statistical uncertainties of the power spectrum measurement for a given survey as well as how two spectra at different multipole and/or redshift bins are correlated with each other. Extending the formulation developed in Scoccimarro et al. (1999) to the tomography case (Takada & Bridle 2007), the covariance matrix of the lensing power spectra is given by

$$\begin{aligned} [C]_{AB} &\equiv \langle P_{(ij)}^{\text{est}}(l_a) P_{(i'j')}^{\text{est}}(l_b) \rangle - P_{(ij)}(l_a) P_{(i'j')}(l_b) \equiv \text{Cov}^{\text{Gaussian}} + \text{Cov}^{\text{NG}} \\ &= \frac{\delta_{ab}^K}{(2l_a + 1)\Delta l f_{\text{sky}}} [P_{(ii')}^{\text{obs}}(l_a) P_{(jj')}^{\text{obs}}(l_a) + P_{(ij')}^{\text{obs}}(l_a) P_{(ji')}^{\text{obs}}(l_a)] + \frac{1}{4\pi f_{\text{sky}}} \int_{|l| \in l_a} \frac{d^2 l}{A(l_a)} \int_{|l'| \in l_b} \frac{d^2 l'}{A(l_b)} T_{(ij'j')}(\mathbf{l}, -\mathbf{l}, \mathbf{l}', -\mathbf{l}'), \end{aligned} \quad (9)$$

where f_{sky} is the sky coverage ($f_{\text{sky}} = \Omega_s/4\pi$). We have shown two contributions to the covariance: the terms in the square brackets constitute the Gaussian contribution, and last term is the non-Gaussian term which is given by the lensing trispectrum T defined as

$$\langle \kappa_{(i)}(\mathbf{l}_1) \kappa_{(j)}(\mathbf{l}_2) \kappa_{(i')}(\mathbf{l}_3) \kappa_{(j')}(\mathbf{l}_4) \rangle \equiv (2\pi)^2 \delta_D(\mathbf{l}_1 + \mathbf{l}_2 + \mathbf{l}_3 + \mathbf{l}_4) T_{(ij'j')}(\mathbf{l}_1, \mathbf{l}_2, \mathbf{l}_3, \mathbf{l}_4). \quad (10)$$

In the Limber approximation, T is a simple projection of the 3D mass trispectrum T_δ given as

$$T_{(ij i' j')}(\mathbf{l}, \mathbf{l}', \mathbf{l}'', \mathbf{l}''') = \int_0^{\chi_H} d\chi W_{(i)}(\chi) W_{(j)}(\chi) W_{(i')}(\chi) W_{(j')}(\chi) \chi^{-6} T_\delta(\mathbf{k}, \mathbf{k}', \mathbf{k}'', \mathbf{k}'''; \chi), \quad (11)$$

with $\mathbf{k} = \mathbf{l}/\chi$ and so on. Finally, the indices A, B in the covariance matrix of Eqn. (9) run over both multipole and redshift bins. For tomography with n_z redshift bins, there are $n_z(n_z + 1)/2$ different spectra available at each multipole. Hence, with n_l multipole bins, the indices A, B take values $A, B = 1, 2, \dots, n_l \times n_z(n_z + 1)/2$. For example, for $n_z = 3$ and $n_l = 100$, the covariance matrix C has dimension 600×600 .

The first term of the covariance matrix (second line on the r.h.s. of Eqn. [9]) represents the Gaussian error contribution ensuring that the two power spectra of different multipoles are uncorrelated via δ_{ab}^k , while the second term gives the non-Gaussian errors includes correlation between power spectra at different l 's. The two terms both scale with sky coverage as $\propto 1/f_{\text{sky}}$ (but see below for an additional dependence in T). Note that the intrinsic ellipticity noise contributes only to the Gaussian errors via $P_{(i)}^{\text{obs}}$, as long as intrinsic alignments of galaxy ellipticities are negligible. It should be also noted that the non-Gaussian term does not depend on the multipole bin width Δl (because $\int d^2\mathbf{l}/A(l) \approx 1$), so increasing Δl only reduces the Gaussian contribution. However, the signal-to-noise ratio and parameter forecasts we will show below do not depend on the multipole bin width if the bin width is not very coarse (also see Scoccimarro et al. 1999 for the related discussion for the case of 3D mass power spectrum).

Figure 1 gives a quick summary of the impact of non-Gaussian errors on the shear power spectrum. The parameters for the cosmological model and lensing survey are described in § 4.1. The shaded boxes around the solid curve show the expected Gaussian errors on the power spectrum for the assumed survey. The shot noise contribution to the Gaussian errors becomes greater than the sample variance at wavenumbers l greater than the intersection of the power spectrum points with the shot noise line (dashed). The horizontal and vertical error bars demonstrate the impact of the non-Gaussian errors on the power spectrum measurements at each multipole bins. There are two effects. First, the neighboring multipole bins are not independent: the width of each horizontal error bar represents the range of multipoles where the cross-correlation coefficient of power spectra (around the central multipole in that bin) is greater than 0.1 (see § 4.4 for the details). Second, the vertical error bars show the increase in the power spectrum measurement uncertainties due to non-Gaussian errors. These are significant over the range $100 \lesssim l \lesssim 10^3$, where (a) nonlinear clustering is important, and (b) sample variance dominates over shot noise.

3.2 Effect of Finite Survey Area: Beat-Coupling Contribution

As pointed out in Hamilton, Rimes & Scoccimarro (2006; also see Rimes & Hamilton 2005 and Sefussati et al. 2006), there is an additional contribution to the covariance arising from the imperfect sampling of the Fourier modes due to a finite survey area, which we will often refer as to the *beat-coupling* contamination. For a finite survey of size L (we will hereafter assume a survey area of $\Omega_s = L^2$ for simplicity), the uncertainty principle tells us that we cannot measure Fourier modes to a better accuracy than $\varepsilon = 2\pi/L$: two modes that differ by $\varepsilon, l \pm \varepsilon$, cannot be distinguished due to the limited resolution⁶. All statistics we measure contains these uncertainties. Therefore we need to allow the trispectrum in the covariance (9) to have the uncertainties given as

$$T(\mathbf{l} + \varepsilon, -\mathbf{l} + \varepsilon', \mathbf{l}' + \varepsilon'', -\mathbf{l}' + \varepsilon''') \quad (12)$$

where all the wavevectors ε with/without primes denote the fundamental modes with magnitude $|\varepsilon| \simeq 2\pi/L$ but can have different orientations. Note that, since the power spectrum depends only on the *length* of wavenumber \mathbf{k} in a statistically homogeneous and isotropic universe, an estimation of the power spectrum of wavenumber l is not affected by the uncertainty principle as long as it is smoothly varying and $l \gg \varepsilon$:

$$P(|\mathbf{l} + \varepsilon|) \simeq P(l). \quad (13)$$

Hence, the Gaussian error term in the covariance (9) is not affected by the beat-coupling contamination.

For the non-Gaussian term, there is a non-vanishing contribution due the beat-coupling effect. Even for $l \gg \varepsilon$, nonlinear clustering predicts non-vanishing correlations between the modes with wavevectors \mathbf{l} and ε . Surprisingly, this effect yields additional contribution to the covariance that are not negligible, as we show below (and as shown by Rimes & Hamilton 2005 for the 3D power spectrum).

3.3 Halo Model Approach for the Covariance

To compute the lensing power spectrum covariance using Eqn. (9), we need to model the mass trispectrum. The model predictions need to describe the non-linear regime of clustering because most of the useful cosmological information in lensing is contained on small angular scales. In this paper, we employ the dark matter halo approach (Seljak 2000; Peacock & Smith 2000; Ma & Fry 2000; Scoccimarro et al. 2001; also see Cooray & Sheth 2002 for a review), where the n -point correlations of the mass distribution are modeled in terms of two separate contributions: correlation of dark matter particles within one halo, and correlations of particles in different halos. In previous work we have found that, up to the 4-point correlation functions, the halo model gives fairly accurate predictions to match N -body simulation results at $\sim 10 - 30\%$ level (Takada & Jain 2002, 2003a,b). For our purpose, the halo model prescription is reasonably adequate; we discuss possible improvements below.

⁶ Note that ε for the fundamental mode is not to be confused with the intrinsic ellipticity, ϵ !

Based on the halo model approach the mass trispectrum is given by

$$T_{\delta}(\mathbf{k}, \mathbf{k}', \mathbf{k}'', \mathbf{k}''') = T_{\delta}^{\text{PT}}(\mathbf{k}, \mathbf{k}', \mathbf{k}'', \mathbf{k}''') + T_{\delta}^{1h}(\mathbf{k}, \mathbf{k}', \mathbf{k}'', \mathbf{k}'''), \quad (14)$$

where T_{δ}^{1h} denotes the 1-halo term and T_{δ}^{PT} denotes the perturbation theory prediction (e.g., Makino et al. 1992; Jain & Bertschinger 1994; also see Bernardeau et al. 2002 for a review). The details of our halo model implementation are given in Takada & Jain (2003a,b). We will calculate the two contributions to T_{δ} given above, and thus estimate the non-Gaussian covariance as the sum of two terms: $\text{Cov}^{\text{NG}} = \text{Cov}^{\text{NG,PT}} + \text{Cov}^{\text{NG,1h}}$.

In Eqn. (14) we have dropped the 2- and 3-halo term contributions. We have thus assumed that the full trispectrum is well approximated by the sum of the 1-halo term and the perturbation theory prediction. Our rationale for this approximation is: (1) The 1-halo term is dominant in the highly non-linear regime, while in the linear regime the Gaussian assumption for the errors is sufficient. (2) For the different halo terms (2-halo term etc.), there are uncertainties in the model, such as the halo exclusion effect (Takada & Jain 2003a; Fosalba et al. 2005). The perturbation theory prediction is an approximate replacement for these multiple-halo terms. Takada & Jain (2003b) showed for example that the lensing three-point functions computed in this manner are in better agreement with the simulations than the standard halo model predictions (1-, 2- plus 3-halo terms).

Let us consider the contribution of the perturbation theory trispectrum to the covariance. As derived in Appendix A, the full PT mass trispectrum (including the fundamental mode uncertainty) can be computed as

$$T_{\delta}^{\text{PT}}(\mathbf{k}_a + \boldsymbol{\varepsilon}'_k, -\mathbf{k}_a + \boldsymbol{\varepsilon}''_k, \mathbf{k}_b + \tilde{\boldsymbol{\varepsilon}}'''_k, -\mathbf{k}_b + \tilde{\boldsymbol{\varepsilon}}''''_k) \approx T_{\delta}^{\text{PT}}(\mathbf{k}_a, -\mathbf{k}_a, \mathbf{k}_b, -\mathbf{k}_b) + 8P_{\delta}^L(k_a)P_{\delta}^L(k_b)P_{\delta}^L(\varepsilon_k)F_2(\boldsymbol{\varepsilon}_k, -\mathbf{k}_a)[F_2(\boldsymbol{\varepsilon}_k, \mathbf{k}_b) + F_2(\boldsymbol{\varepsilon}_k, -\mathbf{k}_b)], \quad (15)$$

where $\boldsymbol{\varepsilon}_k$ with prime superscripts denote the fundamental modes for a given survey and $\boldsymbol{\varepsilon}_k \equiv \boldsymbol{\varepsilon}'_k + \boldsymbol{\varepsilon}''_k$. The function F_2 is the Fourier-space kernel of the 2nd-order density perturbation defined by Eqn. (A3), $P_{\delta}^L(k)$ is the linear-order mass power spectrum and T_{δ}^{PT} is the tree-level PT mass trispectrum. In perturbation theory, $T_{\delta}^{\text{PT}} \sim O([P_{\delta}^L(k)]^3)$ where $k \sim k_a, k_b$, while the beat-coupling term is of order $P_{\delta}^L(k)^2 P_{\delta}^L(\varepsilon_k)$. So the latter is greater than the former if $P_{\delta}^L(\varepsilon_k) > P_{\delta}^L(k)$, which holds for modes of interest for the CDM power spectrum on wavenumber larger than the turnover scale, which are accessible from current and upcoming surveys.

In the ‘‘translinear’’ regime where the beat-coupling contribution is most significant in the covariance, it roughly gives $\text{Cov} \sim P(\varepsilon)P(k)P(k')$ because the kernel $F_2 \sim O(1)$ or equivalently the quantity $\text{Cov}/P(k)P(k') \sim P(\varepsilon) = \text{constant}$. This is consistent with the plateau seen for $k \gtrsim 0.2$ in Fig. 2 in Hamilton et al. (2006). In this regime, the signal-to-noise ratio for the power spectrum amplitude (defined below in § 4.3) ceases to grow with increasing wavenumber (also see Rimes & Hamilton 2005 and Neyrinck et al. 2006 for simulation- and halo model based studies, and Lee & Pen 2008 measurements from the SDSS galaxy power spectrum). In the next section we will show the results for lensing, which are modified by line-of-sight projections.

Substituting Eqn. (15) into Eqn. (9) gives the contribution to the covariance. The angle integration for the beat-coupling terms, combined with the Limber’s approximation, is given by

$$\oint \frac{d\theta \mathbf{k}}{2\pi} F_2(\boldsymbol{\varepsilon}_k, \mathbf{k}) = \frac{6}{7}, \quad (16)$$

so that that the PT trispectrum contribution to the non-Gaussian errors of the lensing covariance can be expressed as

$$\text{Cov}[P_{(ij)}(l_a), P_{(i'j')}(l_b)]^{\text{NG,PT}} \approx \frac{1}{4\pi f_{\text{sky}}} \left[\int_0^{2\pi} \frac{d\theta}{2\pi} T_{(ij i'j')}^{\text{PT}}(l_a, l_b, \cos \theta) + 16 \left(\frac{6}{7}\right)^2 \int d\chi W_{(i)} W_{(j)} W_{(i')} W_{(j')} \chi^{-6} P_{\delta}^L\left(k_a = \frac{l_a}{\chi}\right) P_{\delta}^L\left(k_b = \frac{l_b}{\chi}\right) P_{\delta}^L\left(\varepsilon_k = \frac{2\pi}{L\chi}\right) \right], \quad (17)$$

where

$$T_{(ij i'j')}^{\text{PT}}(l_a, l_b, \cos \theta) = \int d\chi W_{(i)} W_{(j)} W_{(i')} W_{(j')} \chi^{-6} T_{\delta}^{\text{PT}}(\mathbf{k}_a, -\mathbf{k}_a, \mathbf{k}_b, -\mathbf{k}_b; \cos \theta), \quad (18)$$

and $\mathbf{k}_a \cdot \mathbf{k}_b \equiv k_a k_b \cos \theta$. Note that the covariance above depends on the survey size through the prefactor $f_{\text{sky}} = L^2/4\pi = \Omega_s/4\pi$ and the additional dependence of the beat-coupling term on ε_k .

Next let us consider the 1-halo term contribution, which dominates at small angular scales. Although the trispectrum generally depends on four wavevectors, the 1-halo term depends only on the length of each vector since we assume spherical halos. This allows us to make the approximation, even in the presence of the beat-coupling contamination, as

$$\begin{aligned} \text{Cov}[P_{(ij)}(l_a), P_{(i'j')}(l_b)]^{\text{NG,1h}} &= \frac{1}{4\pi f_{\text{sky}}} \int_{|\mathbf{l}| \in l_a} \frac{d^2 \mathbf{l}}{A(l_a)} \int_{|\mathbf{l}'| \in l_b} \frac{d^2 \mathbf{l}'}{A(l_b)} T_{(ij i'j')}^{1h}(|\mathbf{l} + \boldsymbol{\varepsilon}|, |-\mathbf{l} + \boldsymbol{\varepsilon}'|, |\mathbf{l}' + \boldsymbol{\varepsilon}''|, |-\mathbf{l}' + \boldsymbol{\varepsilon}'''|) \\ &\simeq \frac{1}{4\pi f_{\text{sky}}} \int_{|\mathbf{l}| \in l_a} \frac{d^2 \mathbf{l}}{A(l_a)} \int_{|\mathbf{l}'| \in l_b} \frac{d^2 \mathbf{l}'}{A(l_b)} T_{(ij i'j')}^{1h}(l, l, l', l') \\ &= \frac{1}{4\pi f_{\text{sky}}} T_{(ij i'j')}^{1h}(l_a, l_a, l_b, l_b), \end{aligned} \quad (19)$$

where we have assumed that the multipoles of interest, where the non-Gaussian errors are relevant, are greater than the fundamental mode of a given survey: $l_a, l_b \gg \varepsilon = 2\pi/L$, and on the third equality of the r.h.s. we have assume the trispectrum varies smoothly within bins of l . Thus the 1-halo term is not affected by the beat-coupling contamination.

For a given model, we compute the lensing covariance as the sum of the Gaussian contribution, the first term on the r.h.s. of Eqn. (9), and the non-Gaussian contributions, given by $\text{Cov}^{\text{NG,PT}}$ in Eqn. (17) and $\text{Cov}^{\text{NG,1h}}$ in Eqn. (19). As one demonstration of our halo model approach we compare the model predictions for the covariances of angular galaxy power spectrum with the SDSS measurement result of Lee & Pen (2008) in Appendix B, where an encouraging agreement is found.

4 RESULTS

4.1 Model Parameters

To compute the lensing observables, we need to specify a cosmological model and survey parameters. We will forecast below how the non-Gaussian errors degrade parameter determination through measurements of power spectra as a function of survey parameters that are chosen to represent future weak lensing surveys (from both ground and space).

We include all the key parameters that may affect lensing observables within the Λ CDM and dark energy cosmological framework. Our fiducial model is based on the WMAP 5-year results (Komatsu et al. 2008): the density parameters for dark energy, CDM and baryon are $\Omega_{\text{de}} (= 0.74)$, $\Omega_{\text{cdm}} h^2 (= 0.11)$, and $\Omega_{\text{b}} h^2 (= 0.0227)$ (note that we assume a flat universe); the primordial power spectrum parameters are the spectral tilt, $n_s (= 0.963)$, the running index, $\alpha_s (= 0)$, and the normalization parameter of primordial curvature perturbations, $A_s \equiv \delta_c^2 (= 2.41 \times 10^{-9})$ (the values in the parentheses denote the fiducial model). We employ the transfer function of matter perturbations, $T(k)$, with baryon oscillations smoothed out (Eisenstein & Hu 1999), and adopt the primordial power spectrum given in Appendix C in Takada et al. (2006), where the primordial spectrum amplitude is normalized at $k_0 = 0.002 \text{ Mpc}^{-1}$ following the convention in Komatsu et al. (2008). Note that the present-day rms mass fluctuations enclosed within spheres of radius $8h^{-1} \text{ Mpc}$, $\sigma_8 \simeq 0.80$ for our fiducial model. The dark energy equation of state, which governs redshift evolution of the energy density of dark energy together with Ω_{de} , is parametrized as $w(a) = w_0 + w_a(1 - a)$, with fiducial values $w_0 = -1$ and $w_a = 0$.

We model the redshift distribution of galaxies with a function specified by one parameter z_0 (which depends on survey depth):

$$n_s(z; z_0) = n_0 \times 4z^2 \exp\left[-\frac{z}{z_0}\right], \quad (20)$$

where the normalization is fixed by setting $n_0 = 1.18 \times 10^9$ per unit steradian corresponding to $n_0 \simeq 100 \text{ arcmin}^{-2}$. The redshift dependence is same as that assumed in Takada & Jain (2004) or Huterer et al. (2006), but the normalization is fixed. This simple form has nice properties as follows. The mean redshift of source galaxies, z_m , is given by $z_m \equiv \int_0^\infty dz z n_s(z; z_0) / \int_0^\infty dz n_s(z; z_0) = 3z_0$. Thus once the mean redshift is specified, the average number density of galaxies (or equivalently the survey depth) is also specified: e.g., for $z_m = 0.7, 1.0, 1.2$ and 1.5 the corresponding number densities are $\bar{n}_g \equiv \int_0^\infty dz n(z) \simeq 10, 30, 51$ and 100 arcmin^{-2} , respectively. Hence the source distribution above can roughly represent future planned lensing surveys, DES, Subaru Weak Lensing Survey, LSST, and SNAP, simply by adjusting the parameter z_0 (e.g. Hoekstra & Jain 2008 for a review).

The fiducial survey we will assume in the following is a ground-based weak lensing survey that is given by survey area 2000 deg^2 , mean source redshift $z_m = 1$ corresponding to $\bar{n}_g \simeq 30 \text{ arcmin}^{-2}$, and rms intrinsic ellipticity $\sigma_\epsilon = 0.22$. Our fiducial survey roughly resembles the Subaru Weak Lensing Survey (Miyazaki et al. 2006).

4.2 Correlation Coefficients of the Power Spectrum Covariance

The correlation coefficients of the power spectrum covariances quantify the relative strengths of the off-diagonal components to the diagonal components; e.g., the correlation strengths between band powers at different multipole bins for the case of no tomography. The correlation coefficient is defined from Eqn. (9) as

$$r_{AB} \equiv \frac{C_{AB}}{\sqrt{C_{AA}C_{BB}}}. \quad (21)$$

The coefficients are normalized so that $r = 1$ for the diagonal components with $A = B$. For the off-diagonal components with $A \neq B$, $r_{AB} \rightarrow 1$ implies strong correlation between the power spectra of A - and B -th bins, while $r_{AB} = 0$ corresponds to no correlation. As shown in Eqn. (9), the relative importance of the non-Gaussian errors in the power spectrum covariance depends on the bin width of angular multipoles assumed. For larger bin width, the non-Gaussian error contributions get suppressed relative to the Gaussian errors.

Figure 2 shows the correlation coefficients for the fiducial ground-based survey above and the case of no tomography. One can see that the correlation coefficients are well below 0.5 for low multipoles, but increase as one goes to smaller angular scales, because the lensing signal is more affected by non-linear clustering. This result can be compared to the coefficients of the 3D mass power spectrum, where strong correlations, $r \gtrsim 0.5$, can be seen even in the weakly non-linear regime (Scoccimarro et al. 1999; Takahashi et al. in prep.). The weaker correlations in the lensing power spectrum are due to the line-of-sight projections of independent lensing structures at different redshifts, making the weak lensing fields closer to the Gaussian limit.

Although the covariance matrix is symmetric, we have chosen to show different cases in the upper-left and lower-right elements: intrinsic ellipticity contributions to the covariance are included only in the lower-right. Because the shot noise only contributes to the Gaussian terms (diagonal elements) in the covariance matrix (the denominator of Eqn. [21] for r_{AB}), it lowers r . As one considers smaller angular scales where the multipoles lie well in the shot-noise dominated regime, the power spectrum becomes less affected by the non-Gaussian errors for a given survey. Therefore, a survey with smaller number density of source galaxies is relatively less affected by the non-Gaussian errors.

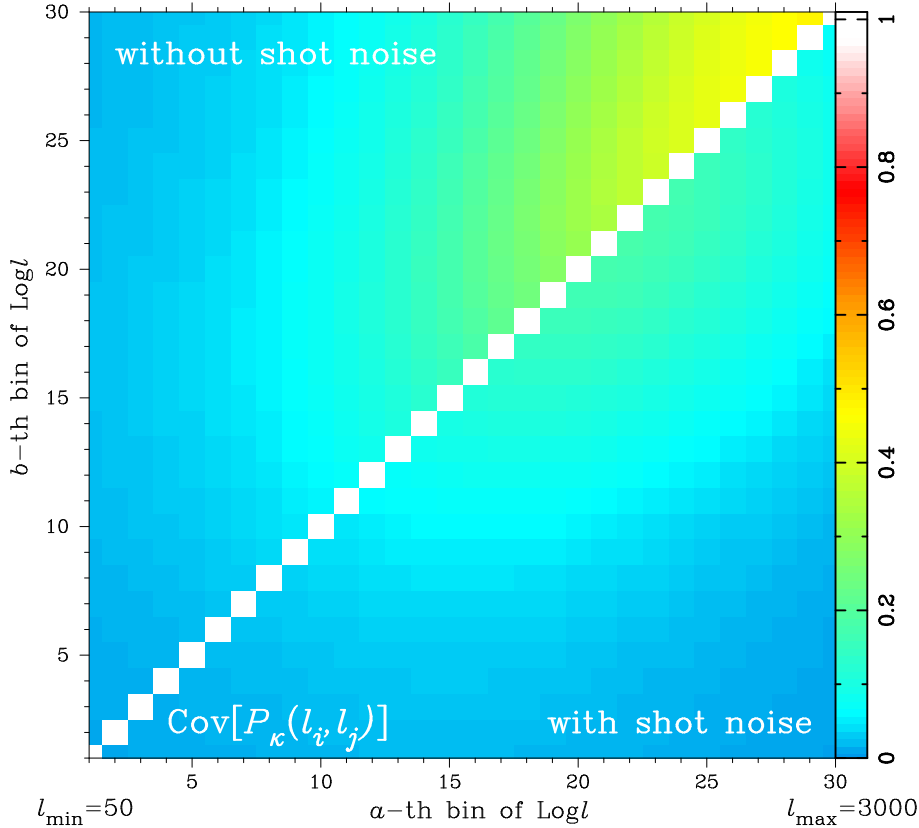


Figure 2. Power spectrum cross-correlation coefficients r_{AB} (see Eqn. [21]) for our fiducial ground-based lensing survey. We consider a single redshift bin (no tomography case), so the indices (A, B) run over 30 logarithmic bins in multipole space over the range $50 \leq l \leq 3000$. The off-diagonal components arise purely from the non-Gaussian errors as shown in Eqn. (9). The upper-left and lower-right off-diagonal components are the results without and with shot noise contamination due to intrinsic ellipticities, respectively. One can see significant correlations at higher l . However, shot noise suppresses the relative importance of non-Gaussian correlations.

We have also checked that our model predictions fairly well reproduce the simulation results for the correlation coefficients shown in Table 2 in Cooray & Hu (2001; also see White & Hu 2000) for multipoles $200 \lesssim l \lesssim 2000$ (when we adjusted our model parameters and multipole bin widths to match those used by these authors).

4.3 Signal-to-Noise for the Lensing Power Spectrum

A useful way to quantify the impact of the non-Gaussian errors is to study the expected signal-to-noise ratio (S/N) for measuring the lensing power spectrum from a given survey, which is independent of the multipole bin widths assumed, as long as the power spectrum does not vary rapidly within the bin widths. The S/N may be defined, using the covariance from Eqn. (9), as

$$\left(\frac{S}{N}\right)^2 = \sum_{A,B} P_{(ij)}(l_a) [C^{-1}]_{AB} P_{(i'j')}(l_b), \quad (22)$$

where C^{-1} is the inverse of the covariance matrix and the summation indices A, B correspond to the dimension of the covariance matrix and run over multipole bins and redshift bins. Note that the power spectra in the above equation represent the lensing signal and do not include the shot noise. The S/N defined above is equivalent to the Fisher information content studied in Tegmark et al. (1997), Rimes & Hamilton (2005) and Lee & Pen (2008). It describes the accuracy in measuring the amplitude of the lensing power spectrum when the shape is completely known.

Figure 3 shows the expected S/N as a function of the maximum multipole l_{\max} , where the power spectrum information over $50 \leq l \leq l_{\max}$ is included in the S/N calculation. The solid curve shows the S/N obtained from our fiducial model prediction for the lensing covariance developed in § 3. It can be compared with the result without the non-Gaussian sample variances, i.e. for the Gaussian error case. As expected, the S/N increases with increasing l_{\max} due to the gain in multipole modes probed. However, the S/N ceases to increase at $l_{\max} \gtrsim 4000$, i.e. little cosmological information is available from these high multipoles, because the shot-noise contamination becomes dominant in the covariances. The impact of the non-Gaussian errors on the S/N also changes with l_{\max} in a characteristic way. For small l_{\max} such as $l_{\max} \lesssim 500$, the effect is small, i.e. the S/N is close to the Gaussian case. For larger l_{\max} where the lensing fields are more affected by the nonlinear regime of mass clustering, the S/N decreases by up to a factor of 2 as explicitly shown in the lower panel. The dotted curve

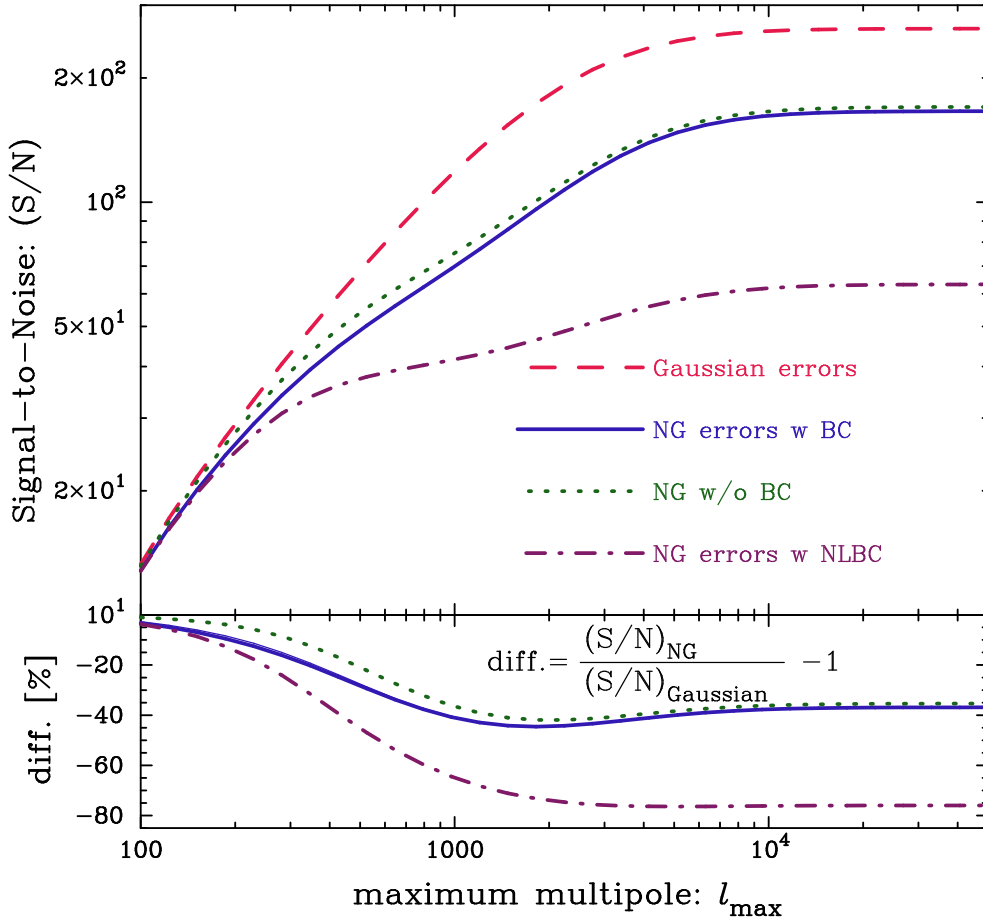


Figure 3. The expected cumulative signal-to-noise ratio (S/N) for the power spectrum is shown as a function of maximum multipole l_{\max} , where the power spectrum information over $50 \leq l \leq l_{\max}$ is included. The dashed and bold-solid curves show the results without and with the non-Gaussian error contribution to the covariance, respectively. The dotted curve shows the result when the beat-coupling contribution is ignored, while the dot-dashed curve is the result when the nonlinear beat-coupling effect is assumed (see text for the details). The survey parameters are as in Figure 1. The lower panel shows the percentage difference relative to the S/N with Gaussian errors.

shows the result obtained when the beat-coupling effect on the covariance due to a finite survey area is ignored. This contribution appears to be non-negligible over a range of l_{\max} , from a few hundreds to ~ 1000 . However, in contrast to the case of 3D mass power spectrum (Rime & Hamilton 2005; Neyrinck et al. 2006), a clear plateau shape in the S/N curves on scales before the shot noise dominated regime cannot be seen. Hence the line-of-sight projection appears to weaken the impact of non-Gaussian errors; lensing at a given angular scale arises from mass fluctuations over a wide range of length scales that may span linear to nonlinear regimes.

Since the magnitude of the beat-coupling effect is not yet well tested from simulations, we also estimate the “worst-case” impact by replacing the linear mass power spectra appearing in Eqn. (17) with the *nonlinear* power spectra. This case, abbreviated NLBC for nonlinear beat coupling, is shown by the dot-dashed curve in Figure 3. Physically this may arise if the mass distribution on highly nonlinear scales, such as the mass distribution within a dark matter halo, is correlated with the mass fluctuations on very large length scales (such correlations are in fact likely to be very weak). The S/N in this case saturates or increases very slowly for $l_{\max} \gtrsim 300$, resulting in a substantial decrease in the S/N (up to a factor of 5).

In Appendix B we compare our halo model predictions with the measurements by Lee & Pen (2008) of the S/N for the angular power spectrum of SDSS galaxies. The standard halo model developed in § 3 is in reasonable agreement with the measurements, consistent with the 10-30% level agreement we found previously between the halo model and simulations (Takada & Jain 2002, 2003b). Even so, we will continue to use the NLBC model to estimate the worst case impact of the non-Gaussian errors. Further detailed studies of the power spectrum covariances for 3D mass and 2D lensing are in preparation (Takahashi et al. and Sato et al. in preparation).

We also estimate the contribution made by the PT trispectrum to the covariance: in Figure 3, the thin-solid curve in the lower panel shows the result when its contribution is ignored. The difference between the bold- and thin-solid curves is barely visible (at $l_{\max} \sim 100$), therefore the PT trispectrum contribution is very small.

The solid curve in Figure 4 shows how the S/N changes with survey depth, i.e. the mean source redshift $z_m \equiv \langle z_s \rangle$. Given a mean source redshift the average number density of source galaxies is specified by Eqn. (20), which in turn determines the shot noise contribution to the covariances. The S/N is greater for a deeper survey, and increases by a factor of 5 between $z_m = 0.6$ and $z_m = 1.5$, because the

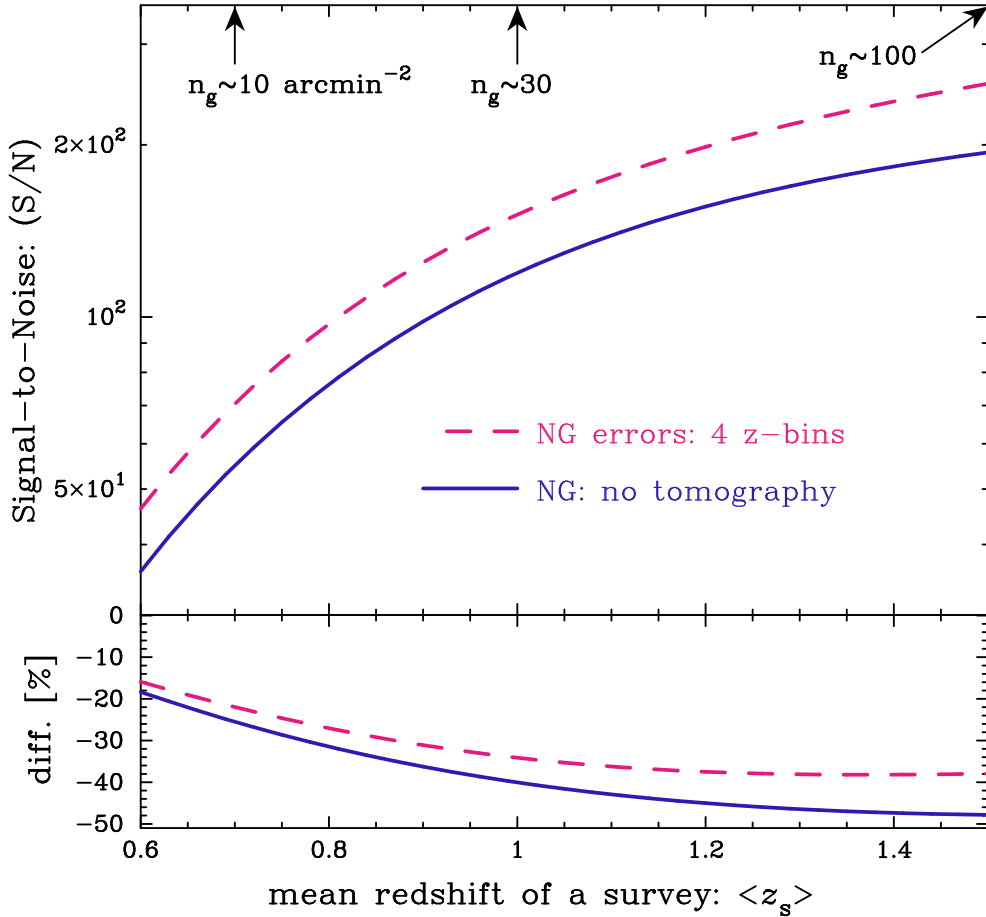


Figure 4. The solid curve shows the dependence of S/N on mean source redshift for the source galaxy distribution given by Eqn. (20), assuming non-Gaussian errors. Power spectrum information over $50 \leq l \leq 3000$ is included, and the survey parameters are as in Figure 1. The x -axis label above the panel shows the corresponding number density of source galaxies. Deeper surveys are more affected by non-Gaussian errors, due to the reduced contribution of shot noise. The dashed curve shows the result for 4 z -bin redshift tomography. The lower panel shows the percentage degradation in S/N compared to the Gaussian errors (with the same number of redshift bins in each case). Adding redshift information not only increases the S/N , but also reduces the impact of the non-Gaussian errors.

lensing signal is higher. However, the impact of non-Gaussian errors on the S/N also becomes more significant for a deeper survey. These results are insensitive to other choices of l_{\max} such as $l_{\max} = 1000$ or 10^4 , as shown in Figure C1.

The dashed curve in Figure 4 demonstrates that adding tomographic redshift information into the lensing power spectrum measurement not only increases the total S/N 's (also see Fig. 5 in Takada & Jain 2004), but also reduces the impact of the non-Gaussian errors. Compared to no tomography case, adding four redshift bins reduces the impact of non-Gaussian errors on the S/N , e.g. to $\sim 35\%$ from $\sim 50\%$ when $l_{\max} = 3000$. Note that four redshift bin tomography is our fiducial survey design for our forecasts of parameter determination shown below.

Finally, in Appendix C we show how the S/N depends on the shot noise and the σ_8 assumed.

4.4 Principal Component Analysis of Lensing Covariance

A principal component analysis of the power spectrum covariance is useful to quantify how the spectra of different multipoles are correlated and how many independent modes exist (see also Scoccimarro et al. 1999 for a similar study for the 3D mass power spectrum). Since the covariance matrix is symmetric by definition, it can always be decomposed as

$$C_{ab} = \sum_m S_{am}(\lambda_m)^2 S_{bm}, \quad (23)$$

where λ_m is the m -th eigenvalue or principal component, $\mathbf{S} = \mathbf{S}^T$, $\sum_c S_{ac}S_{bc} = \delta_{ab}$ and \mathbf{S} is normalized so as to satisfy $\sum_b (S_{ab})^2 = 1$. We consider here no tomography case for simplicity, therefore the dimension of the covariance is given by number of multipole bins. The matrix S_{am} is considered as the projection matrix as it describes how the power in the a -th multipole bin is projected onto the m -th eigenmode. Using this representation, the inverse of the covariance matrix is given by $[C^{-1}]_{ab} = \sum_m S_{am}(1/\lambda_m)^2 S_{bm}$. Hence, the signal-to-noise given by Eqn. (22) can be rewritten as

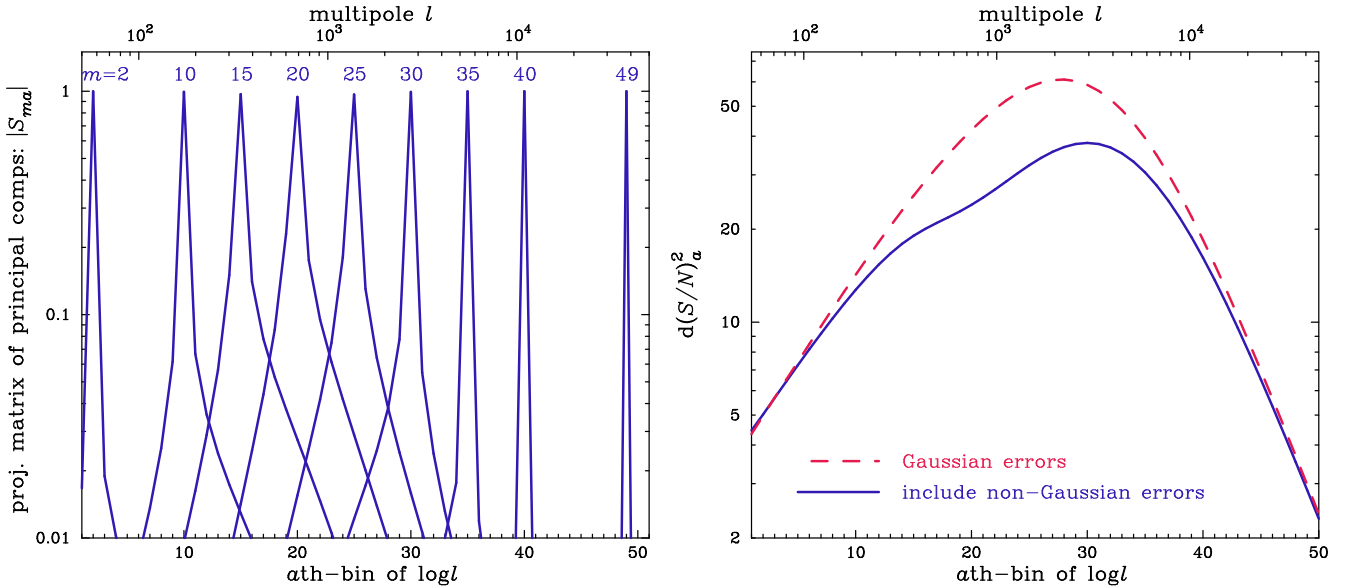


Figure 5. *Left panel:* The projection matrix of S_{am} for the principal component decomposition of the power spectrum covariance is plotted as a function of multipole bins l_a . We employed 50 bins for the multipole binning, i.e. the dimension of S_{am} is 50×50 , and we assumed the survey parameters same as in Figure 1. The absolute value of $|S_{am}|$ for the eight cases of $m = 2, 10, 15, 20, 25, 30, 35, 40, 49$ are shown. The projection matrix around $l \sim 10^3$ gets contributions from a wide range of neighboring multipoles. *Right panel:* The differential contribution to the $(S/N)^2$ at each multipole bin. The dashed and solid curves show the results with the Gaussian and non-Gaussian errors, respectively. The power spectra with $l \sim 2000$ contribute most to the S/N , but are also strongly affected by the non-Gaussian errors. For a survey of 2000 degree², $S/N \gtrsim 3$ can be expected in each multipole bins for $100 \lesssim l \lesssim 2 \times 10^4$. The $d(S/N)^2$ plotted here scales with sky coverage roughly as $d(S/N)^2 \propto f_{\text{sky}}$.

$$\left(\frac{S}{N}\right)^2 = \sum_m \left\{ \frac{1}{\lambda_m} \sum_a S_{am}^P P_a \right\}^2. \quad (24)$$

The equation above expresses the S/N as a sum of contributions from independent eigenmodes.

The projection matrix elements, $|S_{am}|$, for selected values of m between 2 and 50 are shown against the multipole bins in the left panel of Figure 5. Note that elements of S_{am} can be both positive and negative. For the m -th element, $|S_{am}|$ peaks at $a = m$. The projection matrix S_{am} quantifies the correlation between band powers of neighboring bins. The horizontal error bars in Figure 1 are defined as the range of $|S_{am}| \geq 0.1$ around each multipole bins. The projection matrices for the modes around $l \sim 10^3$ are found to have broader tails, reflecting stronger correlations between neighboring multipole bins due to the non-Gaussian errors. For the modes of $l \sim 100$ or $l \gtrsim 4000$, S_{am} has a steep peak at $a = m$, i.e. it is close to the diagonal matrix. At the high l end this is due to the dominance of shot noise over non-Gaussian terms in the covariance. Using this approach, a more sophisticated decorrelating scheme of the band powers may be developed extending the method for the galaxy power spectrum measurement (e.g., Tegmark et al. 2002) to the lensing case.

The right panel of Figure 5 shows the differential contributions of each principal component to the total S/N for the fiducial survey. Note that this plot is shown as a function of the multipole bins rather than the principal components, assuming that the m -th principal component arise mainly from the m -th multipole bin as shown in the left panel. The solid and dashed curves display the results when the non-Gaussian errors are included or ignored, respectively. The power spectrum at $l \sim 3000$ is most accurately measurable for both cases. More generally, a detection of the lensing signal at more than 3σ can be expected over the wide range $100 \lesssim l \lesssim 10^4$ even in the presence of non-Gaussian errors. It should be noted that $(S/N)^2 \propto f_{\text{sky}}$ (for a fixed \bar{n}_g) to good approximation, therefore the result shown here can be scaled to a survey of arbitrary area. Non-Gaussian errors degrade the differential S/N by up to a factor of 2. The vertical error bars at each multipole bin in Figure 1 are computed using: $\sigma(P(l_m))/P(l_m) = \pm[d(S/N)_m^2]^{-1/2}$.

We may summarize the results so far: non-Gaussian errors do affect the lensing power spectrum measurement, and therefore must be included in measurement analyses for ongoing and planned future surveys (see also Semboloni et al. 2007). The impact of non-Gaussian errors depends on various ingredients such as survey parameters, range of multipoles and cosmological parameters (especially σ_8), and these dependencies need to be carefully taken into account if a calibration of the covariance is done based on simulations which may not span the full range of parameters.

4.5 The Impact of Non-Gaussian Errors on Parameter Estimations

In this section we address how the non-Gaussian errors degrade the ability of a given weak lensing survey to constrain cosmological parameters, especially the parameters of dark energy.

To do this, we use the Fisher matrix formalism to estimate accuracies of estimating parameters given the power spectrum measurement.

Cosmological Parameters: Lensing+CMB

	Gaussian	Non-Gauss.	Non-Gauss. w/o BC	Non-Gauss. w NLBC
$\sigma(\Omega_{\text{de}})$	0.018	0.019(6%)	0.019(6)	0.021(17)
$\sigma(\ln A_s)$	0.024	0.025(4%)	0.024(0)	0.024(0)
$\sigma(w_0)$	0.21	0.22(5%)	0.22(5)	0.24(14)
$\sigma(w_a)$	0.61	0.63(3%)	0.62(2)	0.67(10)
$\sigma(n_s)$	0.012	0.012(0%)	0.012(0)	0.012(0)
$\sigma(\alpha_s)$	0.0033	0.0034(3%)	0.0033(0)	0.0034(3)
$\sigma(w_{\text{pivot}})$	0.056	0.061(9%)	0.058(4)	0.065(16)

Table 1. Summary of parameter constraints for lensing tomography with 4 redshift bins, combined with Planck CMB priors. Column 2: assuming Gaussian errors; Column 3: including the non-Gaussian errors; Columns 4 and 5: the errors for the non-Gaussian errors, but ignoring the beat-coupling contribution, and assuming the non-linear beat-coupling (NLBC) contribution to the non-Gaussian errors (see text for the details), respectively. The numbers in round bracket show degradation in the errors compared to the Gaussian case. All errors are 68% confidence-level errors and include marginalization over other parameters. Note that we include power spectrum information over the multipole range $50 \leq l \leq 3000$ and assuming fiducial survey parameters as in Figure 1: $\Omega_{\text{survey}} = 2000 \text{ degree}^2$, $\bar{n}_g \simeq 30 \text{ arcmin}^{-2}$, $\langle z_s \rangle \simeq 1$, and $\sigma_\epsilon = 0.22$.

The parameter forecasts we obtain depend on the fiducial model and are also sensitive to the choice of free parameters. Our fiducial parameters of the cosmological model and lensing survey are given in § 4.1.

Using the covariance matrix (9), the Fisher matrix is given by

$$\mathbf{F}_{\alpha\beta}^{\text{WL}} = \sum_{A,B} \frac{\partial P_{(ij)}(l_a)}{\partial p_\alpha} [\mathbf{C}^{-1}]_{AB} \frac{\partial P_{(i'j')}(l_b)}{\partial p_\beta}, \quad (25)$$

where p_α ($\alpha = 1, 2, \dots$) denotes a set of parameters. The marginalized 1σ error on the α -th parameter p_α is given by $\sigma^2(p_\alpha) = (\mathbf{F}^{-1})_{\alpha\alpha}$, where \mathbf{F}^{-1} is the inverse of the Fisher matrix. It is sometimes useful to consider projected constraints in a two-parameter subspace to see how the two parameters are correlated, and this can be studied following the method described in § 4.1 in Takada & Jain (2004).

Weak lensing alone cannot constrain all the cosmological parameters simultaneously due to parameter degeneracies. However, the parameter degeneracies will be efficiently broken by combining the weak lensing constraints with constraints from the CMB temperature and polarization anisotropies (e.g. Takada & Jain 2004). When computing the Fisher matrix for the CMB, we employ 9 parameters in total: the Thomson scattering optical depth to the last scattering surface, $\tau (= 0.087)$ plus the 8 parameters described in § 4.1. We use the publicly-available CAMB code (Lewis et al. 2000), based on CMBFAST (Seljak & Zaldarriaga 1996), to compute the angular power spectra of temperature anisotropy, C_l^{TT} , E -mode polarization, C_l^{EE} , and their cross correlation, C_l^{TE} . Note that we ignore the B -mode spectra arising from the primordial gravitational waves. Specifically we consider the noise per pixel and the angular resolution of the Planck experiment that were assumed in Eisenstein et al. (1998). In this calculation we use the range of multipoles $10 \leq l \leq 1500$ for C_l^{TT} and C_l^{TE} and use $2 \leq l \leq 1500$ for C_l^{EE} , respectively. Therefore we do not include the ISW effect on the temperature spectra at low multipoles $l \lesssim 10$ which might be affected by a possible contribution of clustered dark energy. To be conservative, however, we do not include the CMB information on dark energy equation of state parameters, w_0 and w_a (also see Takada & Bridle 2007). We first compute the inverse of the CMB Fisher matrix, $\mathbf{F}_{\text{CMB}}^{-1}$, for the 9 parameters in order to obtain marginalized errors on the parameters, and then re-invert a sub-matrix of the inverse Fisher matrix that includes only the rows and columns for the parameters beside w_0 and w_a . The sub-matrix of the CMB Fisher matrix derived in this way describes accuracies of the 7 parameter determination, including degeneracies with the dark energy parameters w_0 and w_a for the hypothetical Planck data sets. The CMB Fisher matrix is added to the lensing Fisher matrix as $\mathbf{F}_{\alpha\beta} = \mathbf{F}_{\alpha\beta}^{\text{WL}} + \mathbf{F}_{\alpha\beta}^{\text{CMB,sub}}$ ($\alpha, \beta = 1, 2, \dots, 9$), where the elements of the CMB Fisher sub-matrix including dark energy parameters w_0 or/and w_a are set to zero.

Table 1 summarizes forecasts for parameter constraints that are expected from lensing tomography of 4 redshift bins (with CMB priors), for our fiducial survey parameters as in Figure 1. We include the power spectrum information over $50 \leq l \leq 3000$ and bin the galaxies such that their number densities in each redshift bin are about equal for a given redshift distribution of galaxies (see Eqn.[20]). Notice that $\sigma(w_{\text{pivot}})$ shows the error in the dark energy equation of state at the best constrained redshift, *pivot redshift* – it is equivalent to the error on a constant $w = w_0$, with w_a fixed to the fiducial value.

One of our main results is given in Column 3 in Table 1, which gives parameter errors including non-Gaussian covariances. These degrade parameter errors typically by less than 10%. This is much smaller than the degradation in the signal-to-noise ratio of power spectrum measurement shown in Figure 4 (a factor of 0.65). Note that the unmarginalized error on each parameter is degraded by roughly similar amount to that for the S/N . If we take the volume of the Fisher error ellipsoid (in our 8-dimensional parameter space) as inversely proportional to the S/N magnitude, then non-Gaussian errors enlarge the Fisher volume by a factor of about 1.54 ($\simeq 1/0.65$). So if all the eight principal axes of the Fisher ellipsoid are equally stretched by the non-Gaussian errors, each parameter error would be degraded only by about 6% [$\simeq (1.54)^{1/8} - 1$], which is the maximum degradation seen in Table 1. In reality, lensing carries information from distance factors, which is not degraded by non-Gaussian errors. Also, non-Gaussian errors change the directions of the principal axes, or equivalently the directions and degrees of parameter degeneracies in parameter space, and we have further combined with the CMB information – both effects can change the results for a particular parameter.

Our results in Table 1 can be compared with Table 4 in Cooray & Hu (2001). They found about a 15% increase in parameter errors due to non-Gaussian errors, with a set of 5 parameters for the Fisher parameter forecasts. Their results can be understood in terms of our

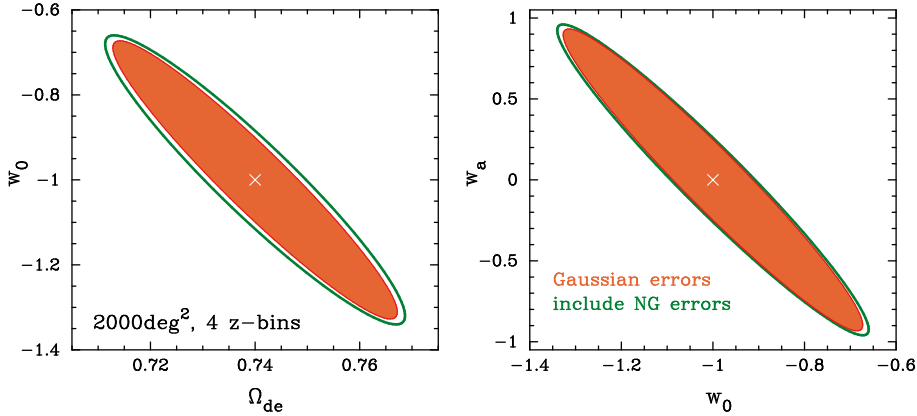


Figure 6. Fisher errors on dark energy parameters, with and without non-Gaussian errors in the lensing covariances. We use lensing tomography with 4 redshift bins and Planck CMB priors. The non-Gaussian errors enlarge the areas of the error ellipses in the subspaces of $(\Omega_{\text{de}}, w_0)$ and (w_0, w_a) by 26% and 12%, respectively. Table 1 gives the one-dimensional marginalized errors on each parameter.

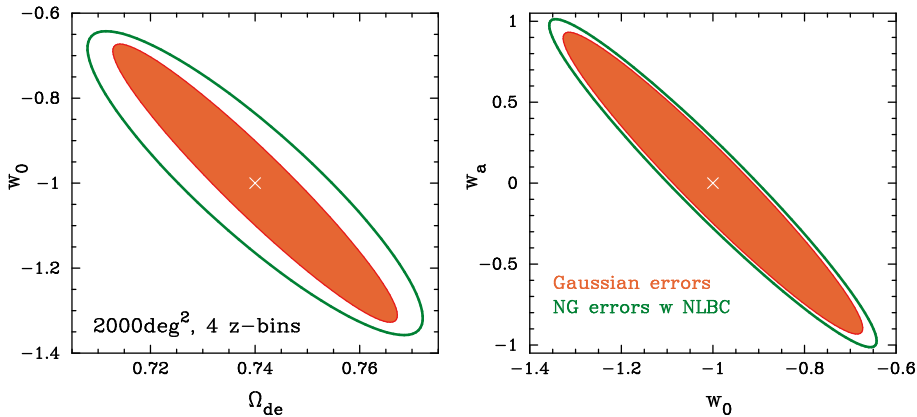


Figure 7. As in the previous figure, but using the non-linear beat-coupling contribution for the non-Gaussian errors. This enlarges the error ellipses (compared to the Gaussian case) by a factor of 2 and $\sim 25\%$, respectively.

findings as follows. First, a fiducial cosmology with higher normalization $\sigma_8 \simeq 1$ was assumed in contrast to our $\sigma_8 \simeq 0.8$. They also considered no tomography case. For these assumptions non-Gaussian errors degrades the S/N by a factor 2 (see Figure C1). Further since they worked with fewer parameters, 5 in contrast to our 8 parameters, the degradation in the marginalized error of each parameter is expected to be $\sim 15\% \simeq 2^{1/5} - 1$. Therefore our results are consistent with theirs.

In summary the impact of non-Gaussian errors on parameter estimations depends on the number of parameters used and the priors used in the analysis. The degradation in the marginalized accuracy of a parameter of interest is generally smaller than that in the total S/N of the power spectrum.

Column 4 in Table 1 shows the errors when ignoring the beat-coupling contribution to the non-Gaussian errors – the effect is very small. Column 5 shows the results when using the nonlinear beat-coupling contribution to the non-Gaussian errors as studied in Figure 3. This model is intended to be an upper bound on the beat-coupling contribution. But even in this case non-Gaussian errors degrade parameter accuracies by less than 20%.

The non-Gaussian errors induce correlations between band powers of the lensing power spectra in multipole as well as redshift space. One may expect that the correlations degrade parameters that are more sensitive to the amplitude of the lensing power spectrum as discussed in Cooray & Hu (2001) and Takada & Bridle (2007). Table 1 does show that the error on Ω_{de} is more degraded than the other parameters (Ω_{de} is most sensitive to the lensing spectrum amplitude for a flat universe, and is also better constrained by lensing than the CMB).

Figures 6 and 7 show how non-Gaussian errors enlarge the projected error ellipses in two-parameter subspaces of dark energy parameters. Our fiducial model for non-Gaussian errors predicts that error ellipses are only slightly enlarged, while including the nonlinear beat-coupling effect enlarges the area of error ellipse by a factor of 2 in the $(\Omega_{\text{de}}, w_0)$ -subspace, and the area by $\sim 25\%$ in the (w_0, w_a) -subspace.

In Figure 8 we study how the impact of the non-Gaussian contribution on the marginalized error of four parameters ($\Omega_{\text{de}}, \ln A_s, w_{\text{pivot}}, w_a$) change with survey depth. It should be noted that, although the parameter errors are estimated for our fiducial survey area (2000 deg^2) combined with the Planck priors, the error shown in the y -axis is multiplied by $f_{\text{sky}}^{1/2} \simeq 0.22$ in order to make it easier to reinterpret the

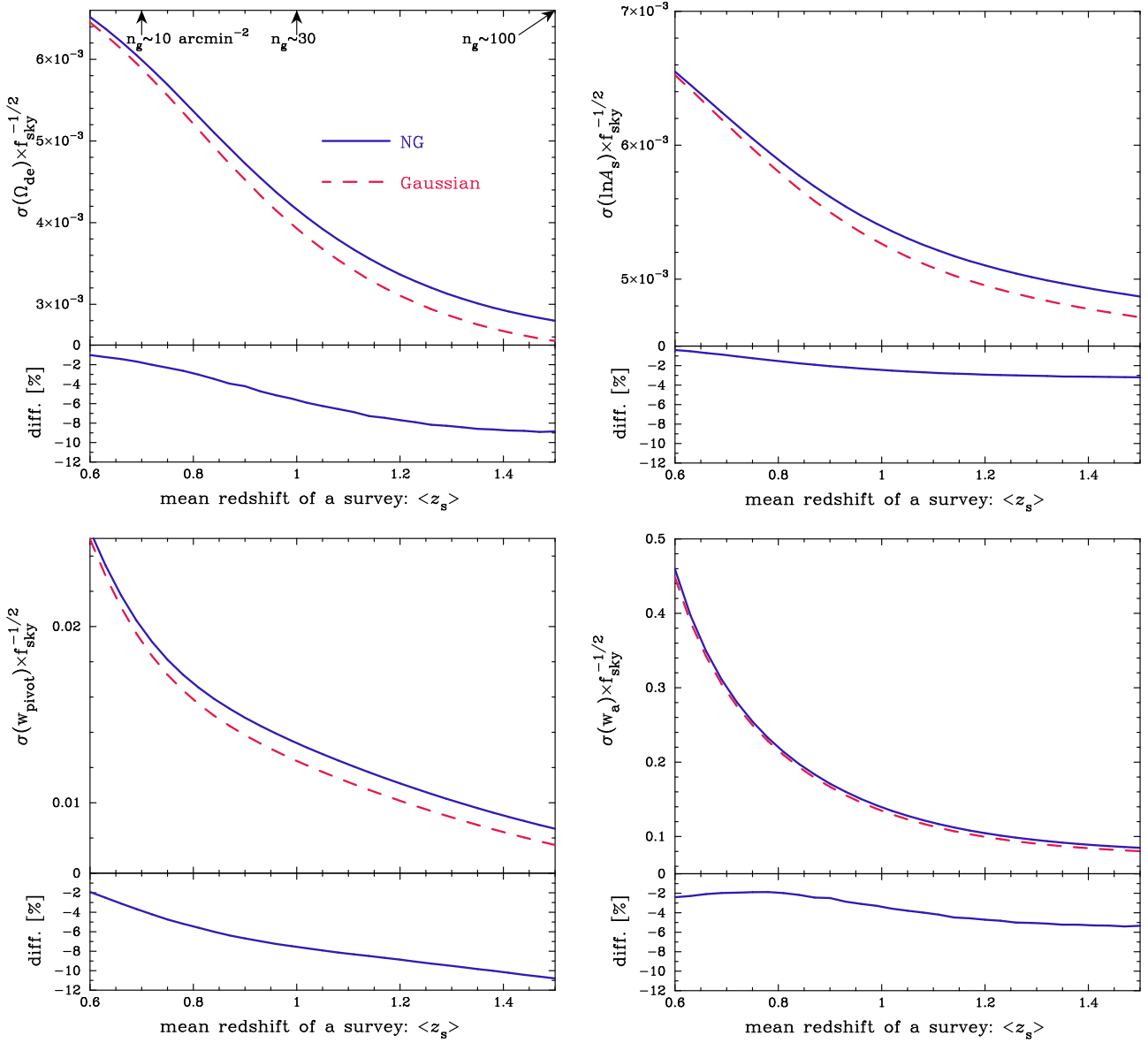


Figure 8. The marginalized 68% errors for the parameters Ω_{de} , $\ln A_s$, w_{pivot} , and w_a as a function of survey depth (as in Figure 4). These errors are obtained from a Fisher matrix analysis combined with the Planck priors. The parameter errors improve with increasing source redshifts, but the error degradation due to non-Gaussian errors become larger.

results shown here for any survey area and depth. The errors roughly scale with $f_{sky}^{-1/2}$ even in the presence of the beat-coupling term in the covariance which does not have this dependence. Although the marginalized errors for these parameters are improved for higher redshift surveys, the impact of the non-Gaussian errors are more significant, as expected from Figure 4. More encouragingly, the error degradation is generally small, less than $\sim 10\%$, for survey depth up to $z_m \simeq 1.5$ we have considered here.

4.6 Degrations in the Presence of Systematic Errors

In reality there are various sources of systematic errors that affect weak lensing measurements. As discussed in several recent studies (Huterer & Takada 2005; Huterer et al. 2006; Ma et al. 2005; Amara & Refregier 2007; Bernstein 2008), stringent control of those systematic errors is required in order to retain the ability of a given weak lensing survey for constraining cosmology. As we have shown, non-Gaussian correlations between the lensing spectra at different multipoles and redshift are important, and themselves depend on the underlying cosmological parameters. On the other hands, the systematic errors generally have a different dependence on multipole and redshift. Therefore including the non-Gaussian covariances into the analysis may help discriminate cosmological signals from systematic errors. This is the issue we hope to address in this subsection.

To do this we model the systematic errors following the method in Huterer et al. (2006): we introduce parameters to describe the

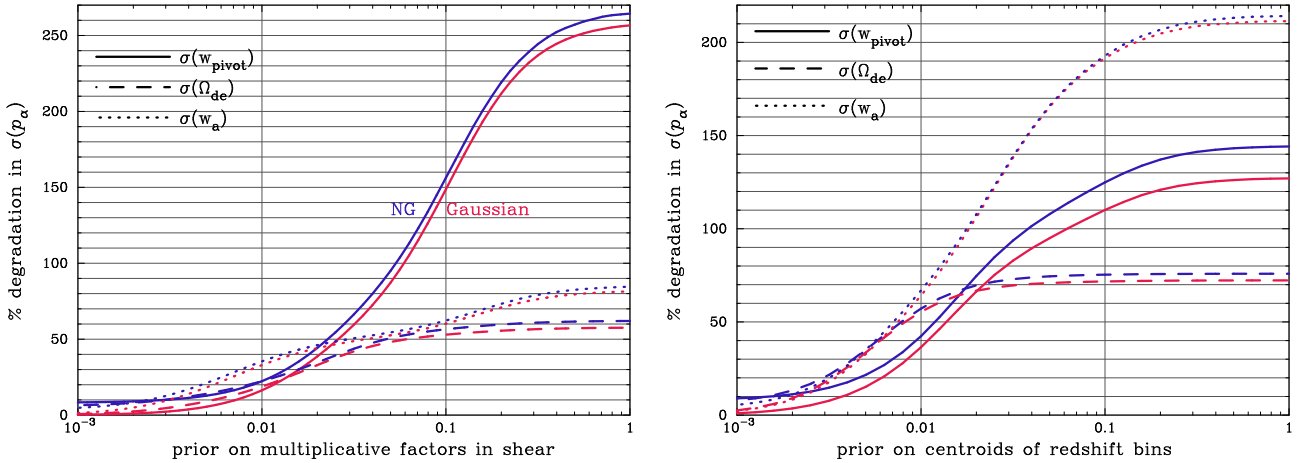


Figure 9. Degradation in the marginalized errors of dark energy parameters Ω_{de} , w_{pivot} and w_a as a function of the priors on the multiplicative shear errors (*Left panel*) or the centroids of redshift bins (*Right*). Predictions for both Gaussian and non-Gaussian covariances are shown. Fiducial survey parameters and four redshift bins are as in Table 1. For the non-Gaussian covariance case, the degradation is relative to the Gaussian error results without the systematic errors, so it includes the degradation caused by non-Gaussian errors as well as systematic errors.

systematic errors and include them as nuisance parameters into the Fisher analysis. In this paper we consider redshift and multiplicative shear errors – the parametrization we use is not generic, but is expected to account for the salient effects.

A multiplicative “calibration bias” in measuring shear is one of typical errors that arise in measuring weak lensing signals (e.g. Massey et al. 2007). The general multiplicative error acts on a galaxy image at some redshift z_s and angular direction θ as $\gamma(z_s, \theta) \rightarrow \gamma(z_s, \theta) [1 + \zeta(z_s, \theta)]$, where ζ is the multiplicative error (bias) in shear. Therefore the lensing spectrum estimated from galaxies in the i - and j -th tomographic redshift bins, $\hat{P}_{(ij)}$, can be biased from the true spectrum $P_{(ij)}$ as

$$\hat{P}_{(ij)}(l) = P_{(ij)}(l) [1 + \zeta_i + \zeta_j]. \quad (26)$$

Here for simplicity we have assumed that the multiplicative errors ζ are not correlated with the cosmological lensing signals, and are dependent only in the tomographic redshift bins, not on multipoles, after averaging. We therefore introduce N_s nuisance parameters for the multiplicative shear errors.

The second systematic error we consider arises from photometric redshift (photo- z) errors. The uncertainties in photo- z estimates – the scatter, bias and fraction of outliers – may significantly degrade the cosmological information of lensing surveys. Statistical errors in photo- z ’s do not by themselves cause problems for lensing tomography because the tomographic redshift bins are derived from an enormous number of redshifts. Rather it is the mean bias in redshift bins that leads to systematic errors in lensing. Therefore we introduce the bias in the centroid of each tomographic redshift bin as a nuisance parameter. We thus introduce N_s nuisance parameters for lensing tomography with N_s redshift bins. To compute the Fisher derivatives for these parameters, we vary each centroid by some small amount δz_s as

$$\langle z_s \rangle_{i\text{-th redshift bin}} \rightarrow \langle z_s \rangle_{i\text{-th redshift bin}} + \delta z_s \quad (27)$$

and then compute the lensing power spectra for the shifted redshift distribution.

We thus have a total of $9 + N_s$ parameters for the two cases, multiplicative shear errors and photo- z ’s errors, and we marginalize over the N_s nuisance parameters in each case by adding the Gaussian priors.

Figure 9 shows the degradation in the marginalized errors of Ω_{de} , w_{pivot} and w_a as a function of the priors on the multiplicative shear errors (left panel) and the redshift bin centroids (right). We compare the results obtained when the non-Gaussian errors are included or ignored. Here “degradation” means that the marginalized error for a given parameter is compared to the error for the Gaussian case without systematic errors: so it shows the effects of both non-Gaussian errors and systematic errors. It is evident from Figure 9 that in the presence of these systematic errors, non-Gaussian errors cause very little degradation. For the multiplicative shear error, with the prior $\sigma(\zeta) = 0.01$ chosen to keep the total degradation below 50%, the differences between the results with and without non-Gaussian errors are about 3, 5 and 2% for $\Omega_{\text{de}0}$, w_{pivot} and w_a , respectively. For the photo- z error, with the prior $\sigma(\delta z_s) = 0.01$, those are about 1, 4 and 2%. These numbers can be compared with the results in Table 1 – the degradations in these dark energy parameters are slightly less significant in the presence of the systematic errors. Therefore, including the cosmological non-Gaussian errors in the covariance slightly mitigates requirements on the control of systematic errors

5 COVARIANCE OF REAL-SPACE SHEAR CORRELATIONS

The real-space correlation function of cosmic shear is another convenient statistic often used in the literature. It has been used in lensing survey measurements (e.g., Fu et al. 2008), as it does not require corrections for survey geometry and masking effects. In this section we study the covariances of the shear correlation functions.

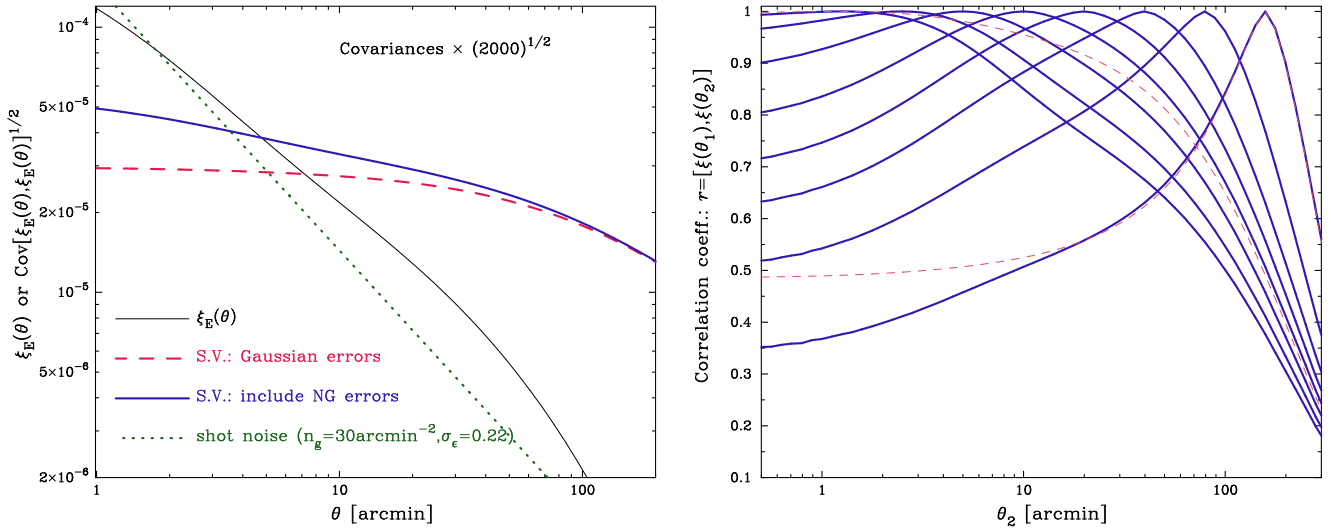


Figure 10. *Left panel:* The diagonal components of the covariance matrix for the shear two-point correlation function as a function of separation angles. The dashed and bold-solid curves are obtained assuming the Gaussian and non-Gaussian errors, respectively. These can be compared with the two-point correlation amplitude ξ_E . The dotted curve is the shot noise contribution due to the intrinsic ellipticities. Survey parameters are as in Figure 1, however, the covariances plotted here are $[\text{Cov} \times 2000]^{1/2}$, effectively corresponding to the case for survey area 1 deg^2 , for illustrative purpose. *Right panel:* The correlation coefficients $r(\theta_1, \theta_2)$ for the two-point correlation function defined as in Eqn. (21). Note that the assumed θ_1 for each curve is given by the value of θ_2 at which $r = 1$. Shot noise is ignored in this plot. The two dashed curves show the results when for the Gaussian error case, for the smallest and largest angles, $\theta_1 \approx 1.2$ and 160 arcminutes, respectively.

The shear E -mode correlation function, $\xi_E(\theta)$, is defined in terms of the lensing power spectrum as

$$\xi_E(\theta) = \int \frac{l dl}{2\pi} P(l) J_0(l\theta), \quad (28)$$

where $J_0(x)$ is the zero-th order Bessel function. Joachimi et al (2008) recently developed a useful formula that allows one to compute the covariances of the real-space correlations in terms of the power spectrum covariance. Extending this method to the case including the non-Gaussian error contributions, the covariance of $\xi_E(\theta)$ can be expressed as

$$\text{Cov}[\xi_E(\theta), \xi_E(\theta')] \simeq \frac{1}{\pi\Omega_s} \int_0^\infty l dl J_0(l\theta) J_0(l\theta') P(l)^2 + \frac{1}{4\pi^2\Omega_s} \int_0^\infty l dl \int_0^\infty l' dl' J_0(l\theta) J_0(l'\theta') \bar{T}(l, l'), \quad (29)$$

where \bar{T} is the angle averaged lensing trispectrum (see the second term on the r.h.s. of Eqn.[9]). We consider no tomography case and ignored shot noise contamination here. The first term on the r.h.s. is the Gaussian error, while the second term gives the non-Gaussian error contribution. There are notable differences between the covariances of the power spectrum and the real-space correlation. Even for a pure Gaussian field, the first term is non-vanishing for the off-diagonal components of the covariance when $\theta \neq \theta'$: i.e., the correlation functions of different angles are always correlated with each other. Also note that the Gaussian covariance does not depend on the bin width of angles. The non-Gaussian errors increase both the diagonal and off-diagonal terms of the covariance.

Thus the cross-correlations between different angles need to be properly taken into account when estimating cosmological parameters from the measured correlation functions. The cosmological interpretation of the measured correlation functions from the CFHT survey (Fu et al. 2008) was made using covariances calibrated with ray-tracing simulations (Semboloni et al. 2007). Simulation based methods are indeed needed to study the covariances; however, accurate calibration of the covariances requires a sufficient number of the realizations (ideally $\gtrsim 100$ realizations to attain % level accuracy at each bin). In addition the simulations are usually done assuming some representative cosmological models, such as the concordance Λ CDM model. Therefore it is computationally expensive to explore covariances in parameter space. Having an analytic method to compute the covariance is useful and complementary to such simulation based methods (also see Schneider et al. 2002).

The left panel of Figure 10 shows our model predictions for the diagonal components of the covariance matrix of the shear correlation function assuming survey parameters as in Figure 1. For illustrative purpose, the covariance is scaled as $[\text{Cov} \times 2000]^{1/2}$, to roughly correspond to a survey with area 1 deg^2 . The covariance amplitude then becomes similar to the shear correlation function (thin solid curve). The dashed and bold-solid curves are the results obtained assuming Gaussian errors (the first term in Eqn. [29]) and also including non-Gaussian errors, respectively. Non-Gaussian errors become more important as one goes to smaller angular scales, $\theta \lesssim 50'$; at the smallest scales $\theta \sim 1'$ currently probed, non-Gaussian errors increase the sample variance by a factor of 1.7. This is smaller than the factor of 4 effect found in Semboloni et al. (2007). The difference may be ascribed partly to the difference in the assumed σ_8 (0.8 vs. 1), leading to $\sim 20\%$ in $\text{Cov}^{1/2}$ (see Figure C1). In addition, it appears that they may have underestimated the Gaussian covariance contribution, which is estimated by integrating the two-point correlations measured from simulations over a finite range of separation angles. Resolving this difference in detail is beyond the scope of this paper, but a detailed study based on simulations would be worth pursuing. The dotted curve is the shot noise

contamination computed as

$$\begin{aligned} \text{Cov}^{\text{shot-noise}}[\xi_E(\theta_i), \xi_E(\theta_j)] &= \frac{2\sigma_\epsilon^2}{N_{\text{pair}}} \\ &\simeq 2.1 \times 10^{-8} \left(\frac{\theta}{1'}\right)^{-2} \left(\frac{\bar{n}_g}{30\text{arcmin}^{-2}}\right)^{-2} \left(\frac{\Omega_s}{1\text{deg}^2}\right)^{-1} \left(\frac{\Delta \ln \theta}{0.46}\right)^{-1} \left(\frac{\sigma_\epsilon}{0.22}\right)^2 \delta_{ij}^K, \end{aligned} \quad (30)$$

where N_{pair} is the total number of galaxy pairs, available from a given survey, that are separated by separation angle θ within bin width $\Delta\theta$. It can be approximately expressed in terms of survey parameters as $N_{\text{pair}} \simeq \pi\theta^2 \Delta \ln \theta \times \bar{n}_g^2 \Omega_s$. The Kronecker delta function δ_{ij}^K is needed as the shot noise contributes only to the diagonal terms of the covariance. A factor of 2 in the numerator of Eqn. (30) accounts for the fact that our definition of σ_ϵ is for the rms intrinsic ellipticities per component while the shear E -mode correlation arises from the sum of the two shear components.

The right panel of Figure 10 shows the correlation coefficients for the two-point function, defined as in Eqn. (21). Note that the shot noise contamination, which only contributes to the diagonal terms of the covariance matrix, is ignored in this plot, and therefore the off-diagonal correlation coefficients are relatively amplified compared to the case including the shot noise. Compared to Figure 2, there are significant correlations between the two-point correlations of different separation angles. Also each curve is asymmetric around the peak, reflecting stronger correlations at smaller scales. For comparison, the dashed curves show the results for the Gaussian error case for two cases of the smallest and largest θ_1 's. Perhaps surprisingly there are even greater cross-correlations than the non-Gaussian error cases, implying the non-Gaussian errors preferentially contribute to the diagonal components.

The results above imply that, if the real-space correlation functions are used to extract cosmological information, inclusion of cross-correlations between different angles in the analysis is critically important (e.g. Schneider et al. 2002). For example, we will use the covariance predictions developed in this paper in order to estimate an upper bound on neutrino masses from the CFHT lensing data, and have indeed found a significant effect of the covariances on the cosmological parameter constraints (Ichiki, Takada & Takahashi 2008).

6 DISCUSSION

In this paper we have studied how non-Gaussian errors due to nonlinear clustering affect measurements of weak lensing power spectra. We have also estimated the degradation in the accuracies of cosmological parameters inferred from future lensing surveys. We pay particular attention to a non-Gaussian contribution that has not been included in the lensing literature so far, the ‘‘beat coupling’’ contribution first studied by Rimes & Hamilton (2005) in 3-dimensional simulations. This term vanishes in the infinite area limit, but for finite survey areas it can dominate the non-Gaussian contribution over some range of angular scales. We use two analytical models to compute it. Both are based on the halo model and must be tested with N-body simulations, but based on preliminary comparisons we expect the simulation results to converge somewhere between the two models (Figure B1 also supports this empirically). Our findings can be summarized as follows.

- Non-Gaussian covariances significantly increase statistical errors on lensing spectra and cause correlations between different multipole bins (see Figures 1 and 2).
- The cumulative signal-to-noise (S/N) ratio, integrated up to a multipole $\gtrsim 1000$, is degraded by up to a factor of 2 (or 5 for the worst case scenario) compared to the Gaussian case (Figure 3). The degradation is smaller for shallower surveys and when including tomographic redshift information (Figure 4).
- For parameter estimations from the lensing spectra, non-Gaussian errors enlarge the volume of the error ellipsoid in parameter space by a factor that is comparable to the S/N degradation.
- However, since lensing impacts multiple parameters the degradation in the marginalized error for individual parameters is much smaller. E.g., for an 8 parameter Fisher analysis the accuracies of dark energy parameters are degraded by less than 10% $\simeq 2^{1/8} - 1$ (or 20%) as shown in Table 1 and Figures 6, 7 and 8.

We have also included two kinds of systematic errors in our analysis: shear calibration and photo- z bias. Since systematic errors in weak lensing generally have a different dependence on multipoles and redshifts, including the non-Gaussian errors in the analysis slightly mitigates requirements on the control of systematic errors (Figure 9). Our model for the power spectrum covariance also allows us to compute the covariance of shear correlation functions, currently used in the analysis of actual measurements. This is presented in Section 5.

The results derived from our analytical method can be used in making realistic forecasts of the ability of future lensing surveys to constrain cosmological parameters. A simulation based study is needed to test our predictions and choose the detailed model (Sato et al, in preparation). The effects of survey geometry and masking can also be estimated from such simulations. However, numerical estimation of the covariances is computationally expensive: more than 1000 realizations of ray-tracing simulations are ideally needed to estimate the covariances at accuracies better than 10% (e.g., see Takahashi et al, in preparation). It would be even more expensive to study the dependence of the covariances on cosmological and survey parameters. Therefore, the analytical method developed here is useful and complementary to such simulation based studies. For example our method allows one to extend the covariances for arbitrary cosmological and survey parameters.

The fact that lensing is significantly affected by non-Gaussianity implies that the power spectrum does not carry all the information contained in lensing fields. Higher-order correlations can be useful in extracting additional cosmological information. For example, combining two- and three-point correlation functions can significantly improve cosmological parameter accuracies (e.g., Takada & Jain 2004). However, one has to properly take into account covariances of higher-order moments by including non-Gaussian errors. This requires going up to 6-point correlations for the bispectrum. We have found that parameter constraints from bispectrum tomography are degraded more

by non-Gaussian covariances than for the power spectrum. Combining the power spectrum and bispectrum is still powerful in breaking parameter degeneracies (Takada & Jain, in preparation).

Finally, we comment on the possibility of combining *all* observables available from multicolor imaging surveys. Besides the lensing power spectra, there are various observables that probe large-scale structure: counting statistics of galaxy clusters, baryon acoustic oscillations, the full galaxy angular correlation functions, galaxy-lensing cross-correlation, and so on. Even though these probe the same cosmic mass density field, combining these observables can improve accuracies on cosmological parameter (for example, see Takada & Bridle 2007). Several open questions remain on strategies for combining observables in the presence of systematic errors. To address such issue quantitatively, all covariances between the observables used have to be correctly taken into account. Such a study is challenging, but will be needed to exploit the full potential of future surveys to constrain the nature of dark energy or possible modifications of gravity.

We are very grateful to I. Kayo and R. Scoccimarro for invaluable discussions and comments. We also thank G. Bernstein, S. Bridle, D. Dolney, T. Hamana, K. Ichiki, M. Jarvis, J. Lee, M. Kilbinger, M. Sato, E. Sefusatti, E. Semboloni, P. Schneider and N. Yoshida for useful discussions. We also thank the Lorentz Center at University of Leiden in Netherlands and IUCAA for their warm hospitality while this work was initiated. MT also thanks the members at Astronomy Department of University of Pennsylvania for their warm hospitality. This work was in part supported by World Premier International Research Center Initiative (WPI Initiative), MEXT, Japan, by Grand-in-Aid for Scientific Research on Priority Area No. 467 “Probing Dark Energy through an Extremely Wide and Deep Survey with Subaru Telescope” and on young researchers (Nos. 17740129 and 20740119) as well as by Grand-in-Aid for the 21st Century Center of Excellence program “Exploring New Science by Bridging Particle-Matter Hierarchy” at Tohoku University. BJ is supported in part by NSF grant AST-0607667.

APPENDIX A: DERIVATION OF THE BEAT-COUPLING CONTRIBUTION TO THE LENSING COVARIANCE

In this section we derive the beat-coupling contribution to the power spectrum covariance in more detail (also see Hamilton et al. 2006 and Sefusatti et al. 2006).

Let us begin by recalling the definition of the 3D mass trispectrum in terms of the mass fluctuation field $\delta_m(\mathbf{k})$:

$$\langle \delta_m(\mathbf{k}_1)\delta_m(\mathbf{k}_2)\delta_m(\mathbf{k}_3)\delta_m(\mathbf{k}_4) \rangle \equiv (2\pi)^3 \delta_D(\mathbf{k}_{1234}) T_\delta(\mathbf{k}_1, \mathbf{k}_2, \mathbf{k}_3, \mathbf{k}_4), \quad (\text{A1})$$

where we have introduced notation such as $\mathbf{k}_{1234} \equiv \mathbf{k}_1 + \mathbf{k}_2 + \mathbf{k}_3 + \mathbf{k}_4$, and the Dirac delta function imposes the condition that the four wavevectors $\mathbf{k}_1, \dots, \mathbf{k}_4$ form a closed 4-point configuration in Fourier space. According to perturbation theory (e.g. see Bernardeau et al. 2002 for a thorough review), the mass trispectrum can be expressed in terms of the linear mass power spectrum as

$$\begin{aligned} T_\delta^{\text{PT}}(\mathbf{k}_1, \mathbf{k}_2, \mathbf{k}_3, \mathbf{k}_4) = & 4 \left[F_2(\mathbf{k}_{12}, -\mathbf{k}_1) F_2(\mathbf{k}_{12}, \mathbf{k}_3) P_\delta^L(k_{12}) P_\delta^L(k_1) P_\delta^L(k_3) + F_2(\mathbf{k}_{12}, -\mathbf{k}_1) F_2(\mathbf{k}_{12}, \mathbf{k}_4) P_\delta^L(k_{12}) P_\delta^L(k_1) P_\delta^L(k_4) \right. \\ & + F_2(\mathbf{k}_{12}, -\mathbf{k}_2) F_2(\mathbf{k}_{12}, \mathbf{k}_3) P_\delta^L(k_{12}) P_\delta^L(k_2) P_\delta^L(k_3) + F_2(\mathbf{k}_{12}, -\mathbf{k}_2) F_2(\mathbf{k}_{12}, \mathbf{k}_4) P_\delta^L(k_{12}) P_\delta^L(k_2) P_\delta^L(k_4) \\ & + F_2(\mathbf{k}_{13}, -\mathbf{k}_1) F_2(\mathbf{k}_{13}, \mathbf{k}_2) P_\delta^L(k_{13}) P_\delta^L(k_1) P_\delta^L(k_2) + F_2(\mathbf{k}_{13}, -\mathbf{k}_1) F_2(\mathbf{k}_{13}, \mathbf{k}_4) P_\delta^L(k_{13}) P_\delta^L(k_1) P_\delta^L(k_4) \\ & + F_2(\mathbf{k}_{13}, -\mathbf{k}_3) F_2(\mathbf{k}_{13}, \mathbf{k}_2) P_\delta^L(k_{13}) P_\delta^L(k_3) P_\delta^L(k_2) + F_2(\mathbf{k}_{13}, -\mathbf{k}_3) F_2(\mathbf{k}_{13}, \mathbf{k}_4) P_\delta^L(k_{13}) P_\delta^L(k_3) P_\delta^L(k_4) \\ & + F_2(\mathbf{k}_{14}, -\mathbf{k}_1) F_2(\mathbf{k}_{14}, \mathbf{k}_2) P_\delta^L(k_{14}) P_\delta^L(k_1) P_\delta^L(k_2) + F_2(\mathbf{k}_{14}, -\mathbf{k}_1) F_2(\mathbf{k}_{14}, \mathbf{k}_3) P_\delta^L(k_{14}) P_\delta^L(k_1) P_\delta^L(k_3) \\ & \left. + F_2(\mathbf{k}_{14}, -\mathbf{k}_4) F_2(\mathbf{k}_{14}, \mathbf{k}_2) P_\delta^L(k_{14}) P_\delta^L(k_4) P_\delta^L(k_2) + F_2(\mathbf{k}_{14}, -\mathbf{k}_4) F_2(\mathbf{k}_{14}, \mathbf{k}_3) P_\delta^L(k_{14}) P_\delta^L(k_4) P_\delta^L(k_3) \right] \\ & + 6 \left[F_3(\mathbf{k}_1, \mathbf{k}_2, \mathbf{k}_3) P_\delta^L(k_1) P_\delta^L(k_2) P_\delta^L(k_3) + F_3(\mathbf{k}_1, \mathbf{k}_2, \mathbf{k}_4) P_\delta^L(k_1) P_\delta^L(k_2) P_\delta^L(k_4) + 3 \text{ perms.} \right], \quad (\text{A2}) \end{aligned}$$

where the kernels F_2 and F_3 are given by

$$F_2(\mathbf{k}_1, \mathbf{k}_2) = \frac{5}{7} + \frac{1}{2} \left(\frac{k_1}{k_2} + \frac{k_2}{k_1} \right) \frac{\mathbf{k}_1 \cdot \mathbf{k}_2}{k_1 k_2} + \frac{2}{7} \frac{(\mathbf{k}_1 \cdot \mathbf{k}_2)^2}{k_1^2 k_2^2} \quad (\text{A3})$$

$$F_3(\mathbf{k}_1, \mathbf{k}_2, \mathbf{k}_3) = \frac{1}{54} \left[7 \frac{\mathbf{k}_{123} \cdot \mathbf{k}_1}{k_1^2} F_2(\mathbf{k}_2, \mathbf{k}_3) + \left\{ 7 \frac{\mathbf{k}_{123} \cdot \mathbf{k}_{23}}{k_{23}^2} + 2 \frac{k_{123}^2 (\mathbf{k}_{23} \cdot \mathbf{k}_1)}{k_{23}^2 k_1^2} \right\} G_2(\mathbf{k}_2, \mathbf{k}_3) + 2 \text{ perms.} \right] \quad (\text{A4})$$

with another kernel G_2 defined as

$$G_2(\mathbf{k}_1, \mathbf{k}_2) \equiv \frac{3}{7} + \frac{1}{2} \left(\frac{k_1}{k_2} + \frac{k_2}{k_1} \right) \frac{\mathbf{k}_1 \cdot \mathbf{k}_2}{k_1 k_2} + \frac{4}{7} \frac{(\mathbf{k}_1 \cdot \mathbf{k}_2)^2}{k_1^2 k_2^2}. \quad (\text{A5})$$

Note that, due to the condition $\mathbf{k}_1 + \mathbf{k}_2 + \mathbf{k}_3 + \mathbf{k}_4 = \mathbf{0}$, there are many other ways to express the mass trispectrum (A2). For convenient purpose of our following discussion, we wrote down the mass trispectrum such that all the term has arguments of \mathbf{k}_{1a} where $a = 2, 3$ or 4.

The covariance of the mass power spectra of two wavenumbers k and k' arises from the 4-point correlations of δ_m with specific configurations in Fourier space: $\langle P_\delta(k) P_\delta(k') \rangle = \langle \delta_m(\mathbf{k}) \delta_m(-\mathbf{k}) \delta_m(\mathbf{k}') \delta_m(-\mathbf{k}') \rangle$, because of $P_\delta(k) = \langle \delta_m(\mathbf{k}) \delta_m(-\mathbf{k}) \rangle$ and so on. Note that, even for the diagonal terms of the covariance where $k = k'$, the two vectors \mathbf{k} and \mathbf{k}' generally differ in direction. As discussed in § 3.2, for any survey of a finite sky or volume coverage, we cannot measure Fourier modes to a better accuracy than the fundamental model of the survey, say $\varepsilon_k = 2\pi/D$, where D is a linear scale of the survey region: two modes that differ by ε_k cannot be in practice distinguished due to the limited resolution. Taking into account this uncertainty, the PT trispectrum contribution to the non-Gaussian part of the mass power spectrum covariance arises from the following mass trispectrum (also see Hamilton et al. 2006):

$$\text{Cov}^{\text{NG,PT}}[P_\delta(k), P_\delta(k')] \leftarrow T_\delta^{\text{PT}}(\mathbf{k} + \varepsilon'_k, -\mathbf{k} + \varepsilon''_k, \mathbf{k}' + \varepsilon'''_{k'}, -\mathbf{k}' + \varepsilon''''_{k'}), \quad (\text{A6})$$

where the vectors ε_k with prime superscripts denote the fundamental modes of amplitude $2\pi/D$.

Assuming the case that the modes of interest are much greater than the fundamental modes, e.g. $k, k' \gg \varepsilon'_k$, substituting Eqn. (A6) into Eqn. (A2) yields

$$T_\delta^{\text{PT}}(\mathbf{k} + \varepsilon'_k, -\mathbf{k} + \varepsilon''_k, \mathbf{k}' + \varepsilon'''_k, -\mathbf{k}' + \varepsilon''''_k) \approx T_\delta^{\text{PT}}(\mathbf{k}, -\mathbf{k}, \mathbf{k}', -\mathbf{k}') + 4P_\delta^L(\varepsilon_k)P_\delta^L(k)P_\delta^L(k') \left[F_2(\varepsilon_k, -\mathbf{k})F_2(\varepsilon_k, \mathbf{k}') + F_2(\varepsilon_k, -\mathbf{k})F_2(\varepsilon_k, -\mathbf{k}') + F_2(\varepsilon_k, \mathbf{k})F_2(\varepsilon_k, \mathbf{k}') + F_2(\varepsilon_k, \mathbf{k})F_2(\varepsilon_k, -\mathbf{k}') \right], \quad (\text{A7})$$

where $\varepsilon_k \equiv \varepsilon'_k + \varepsilon''_k$. In the derivation above, we have used the fact that the first four terms in the square bracket on the r.h.s. of Eqn. (A2) can be computed as $F_2(\mathbf{k}_{12}, -\mathbf{k}_1)P_\delta^L(k_{12})P_\delta^L(k_1) \approx F_2(\varepsilon' + \varepsilon''_k, -\mathbf{k})P_\delta^L(|\varepsilon'_k + \varepsilon''_k|)P_\delta^L(k)$ when $\mathbf{k}_1 = \mathbf{k} + \varepsilon'$ and $\mathbf{k}_2 = -\mathbf{k} + \varepsilon''$, which are thus proportional to $P(\varepsilon_k)$ and greater than the other terms because $F_2 \sim O(1)$ and $P_\delta^L(\varepsilon_k) \gg P_\delta^L(k)$ for a CDM spectrum. The other terms are computed as $F_2(\mathbf{k}_{13}, -\mathbf{k}_1)P_\delta^L(k_{13})P_\delta^L(k_1) \approx F_2(|\mathbf{k} + \mathbf{k}'|, -\mathbf{k})P_\delta^L(|\mathbf{k} + \mathbf{k}'|)P_\delta^L(k)$ under the assumption $k \gg \varepsilon_k$, and are rewritten as the form of the standard trispectrum contribution, $T_\delta^{\text{PT}}(\mathbf{k}, -\mathbf{k}, \mathbf{k}', -\mathbf{k}')$. By integrating the equation above over angles of wavevectors \mathbf{k} and \mathbf{k}' , combined with the Limber's approximation and the lensing projection, the contribution to the lensing covariance given by Eqn. (17) can be obtained.

Although a rather mathematical derivation of the beat-coupling was described above, we will in the following make a more intuitive explanation on the beat-coupling effect within the framework of the halo model approach. In the halo model picture, the mass density fluctuation field of a given wavevector \mathbf{k} is expressed as the sum of the mass fluctuations in the highly nonlinear regime, confined within one halo, and the mass fluctuations in the weakly nonlinear regime arising from the halo distribution, which we here refer as to the 1-halo term, δ_m^{1h} , and the perturbation theory contribution, δ_m^{PT} , respectively:

$$\delta_m(\mathbf{k}) = \delta_m^{\text{PT}}(\mathbf{k}) + \delta_m^{1h}(\mathbf{k}). \quad (\text{A8})$$

In the presence of the fundamental mode uncertainty the mass fluctuations in the weakly nonlinear regime contain contributions of physical correlations between the modes of \mathbf{k} and ε arising from nonlinearities of gravitational clustering. More precisely, based on the perturbation theory, the density fluctuation field δ_m^{PT} can be expanded as

$$\begin{aligned} \delta_m^{\text{PT}}(\mathbf{k} + \varepsilon_k) &= \delta_m^{(1)}(\mathbf{k} + \varepsilon_k) + \delta_m^{(2)}(\mathbf{k} + \varepsilon_k) + \delta_m^{(3)}(\mathbf{k} + \varepsilon_k) + \dots \\ &\approx \delta_m^{(1)}(\mathbf{k}) + \int \frac{d^3\mathbf{q}}{(2\pi)^3} F_2(\mathbf{q}, \mathbf{q} - \mathbf{k} - \varepsilon_k) \delta_m^{(1)}(\mathbf{q}) \delta_m^{(1)}(\mathbf{k} + \varepsilon_k - \mathbf{q}) \\ &\quad + \int \frac{d^3\mathbf{q}_1}{(2\pi)^3} \frac{d^3\mathbf{q}_2}{(2\pi)^3} F_3(\mathbf{q}_1, \mathbf{q}_2, \mathbf{k} + \varepsilon_k - \mathbf{q}_1 - \mathbf{q}_2) \delta_m^{(1)}(\mathbf{q}_1) \delta_m^{(1)}(\mathbf{q}_2) \delta_m^{(1)}(\mathbf{k} + \varepsilon_k - \mathbf{q}_1 - \mathbf{q}_2) + \dots, \end{aligned} \quad (\text{A9})$$

where $\delta_m^{(1)}$, $\delta_m^{(2)}$ and $\delta_m^{(3)}$ are the linear-, 2nd- and 3rd-order contributions of the mass fluctuations in the perturbative expansion (e.g., see Jain & Bertschinger 1994), and in the second equality on the r.h.s. of the equation above we have used that the linear-order fluctuations are only slowly varying with wavenumbers for a CDM model, $\delta_m^{(1)}(\mathbf{k} + \varepsilon_k) \approx \delta_m^{(1)}(\mathbf{k})$. Thus gravitational instability that doesn't have any characteristic scale predicts that all the fluctuations of different scales are coupled to each other. In particular, the 2nd-order density fluctuations are found to contain contributions arising from the correlations between the fluctuations of \mathbf{k} and the fundamental mode: $F_2(\mathbf{k}, \varepsilon_k) \delta_m^{(1)}(\mathbf{k}) \delta_m^{(1)}(\varepsilon_k)$ when $\mathbf{q} = \mathbf{k}$. Such contributions to the power spectrum covariance indeed arise after taking the ensemble average such as $\langle \delta_m^{(1)}(-\mathbf{k}) \delta_m^{(1)}(\mathbf{q}) \delta_m^{(1)}(\mathbf{k} + \varepsilon_k - \mathbf{q}) \rangle$ in the covariance calculation. Thus the beat-coupling contribution is caused by the physical correlation between the mass fluctuations of large- and small-distance scales as predicted by the perturbation theory of mass clustering. In other words, if there are no such correlations, e.g. in the case of the linear regime, the power spectrum measured from a finite survey is not influenced by the fundamental mode uncertainty.

On the other hand, the highly nonlinear mass fluctuations are unlikely to be affected by the fundamental mode uncertainty as follows. Since the mass fluctuations in the highly nonlinear regime are very likely to lie inside a halo, the self-gravitating bound object, the mass distribution within the halo would be sufficiently decoupled from and unaffected by large-scale fluctuations, for example as in the stable clustering ansatz where the highly nonlinear fluctuations are assumed to be totally decoupled from the Hubble flow. Therefore the 1-halo trispectrum contribution to the power spectrum covariance is unlikely to be contaminated by the beat-coupling effect. Note that, although the 1-halo term also depends on the halo mass function in addition to the mass distribution inside a halo, the mass function can be mapped out from the *linear-order* mass fluctuations to zero-th order approximation, as done in the Press-Schechter prescription, and therefore would not be affected by the fundamental mode uncertainty according to the rationale discussed in the previous paragraph.

APPENDIX B: COVARIANCES OF ANGULAR MASS POWER SPECTRUM: COMPARISON OF OUR MODEL PREDICTION WITH LEE & PEN

In this appendix, as one check of our model, we will show the comparison of our model predictions with the SDSS angular galaxy power spectrum recently measured in Lee & Pen (2008).

The formulation we have developed in this paper is readily applied to the angular power spectrum of mass clustering if the redshift weight function for lensing, $W_{(i)}(\chi)$ (e.g. see Eqn. [6]), is replaced with the selection function of a given galaxy survey as

$$W_{(i)}(\chi) \rightarrow p_g(z) \frac{dz}{d\chi}, \quad (\text{B1})$$

where $p_g(z)$ is the selection function: $p_g(z)$ is unity if z is in the range of redshifts surveyed, otherwise zero. Note that the selection function should be normalized so as to satisfy $\int dz p_g(z) = 1$.

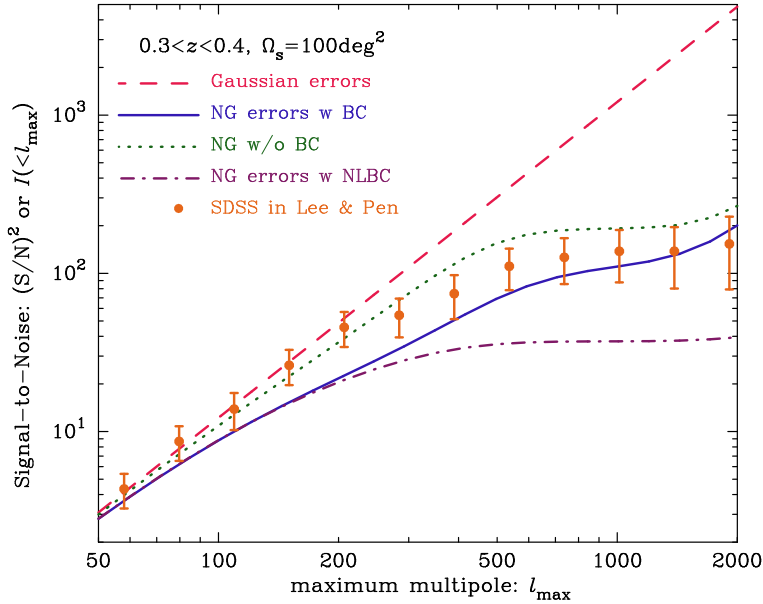


Figure B1. Comparison of our model predictions with the SDSS measurements of Lee & Pen (2008), for the cumulative signal-to-noise (or the information content) of the mass or galaxy angular power spectrum, respectively. The survey parameters are taken to resemble the SDSS result. As in Figure 3, the solid and dotted curves are the results obtained including the non-Gaussian errors with and without the beat-coupling effect, while the dashed curve is the result for the Gaussian error case, which scales as $(S/N)^2 \propto l_{\max}^2$. Our model predictions taking account of non-Gaussian errors are in fairly good agreement with the measurement result, even though there is uncertainty due to galaxy bias (see text). The dot-dashed curve shows the result assuming the nonlinear beat-coupling, which is smaller than the measurement by a factor of a few.

Figure B1 shows the cumulative signal-to-noise ratio expected for measuring angular power spectrum of the mass distribution over multipole range $2 \leq l \leq l_{\max}$ as a function of the maximum multipole l_{\max} , assuming a survey with area $\Omega_s = 100 \text{ deg}^2$ and redshift coverage $0.3 \leq z \leq 0.4$ that are chosen to resemble the survey parameters in Lee & Pen. Here we didn't include the shot noise contamination such that our $(S/N)^2$ given by Eqn. (22) becomes equivalent to the Fisher information content I studied in Lee & Pen, where the shot noise contamination due to discrete galaxy distribution is subtracted. It should be also worth noting that the galaxy bias uncertainty may not so largely change our results for mass power spectrum, as the bias factor to some extent cancels out in the $(S/N)^2$ evaluation. For the linear bias case, the $(S/N)^2$'s for mass and galaxy distribution are exactly equivalent as $P_g = b^2 P_\delta$ and $[\text{Cov}(P_g)]^{-1} = b^{-4} [\text{Cov}(P_\delta)]^{-1}$.

The solid and dotted curves show our model predictions including non-Gaussian errors, but with and without the beat-coupling effect, respectively, while the dashed curve show the result for the Gaussian error, which scales as l_{\max}^2 in the absence of shot noise. Several interesting points can be found from this plot. First, the beat-coupling effect appears to be more significant for this angular power spectrum than the lensing spectrum, because the angular power spectrum has a much narrower redshift coverage, i.e. less line-of-sight projection. More precisely, since the comoving angular diameter distance to $z \simeq 0.35$ is $\chi \simeq 1400 \text{ Mpc}$ for our fiducial cosmology, the translinear regime of $k \simeq [0.1, 1] \text{ Mpc}^{-1}$, where the beat-coupling is expected to be significant (Rimes & Hamilton 2005), appears over a wider range of multipoles $l \simeq k\chi \simeq [140, 1400]$. For the lensing case, the translinear regime signature is smeared out by the projection over a wider range of redshifts. Second, very encouragingly, our model predictions fairly well reproduce the measurement results. On the other hand, the dot-dashed curve show the the result obtained assuming the nonlinear beat-coupling effect. This prediction underestimates the measurement by a factor of 3 on $l_{\max} \gtrsim 500$, implying an overestimation of the beat-coupling effect in this prescription.

APPENDIX C: DEPENDENCE OF THE LENSING S/N ON OTHER PARAMETERS

In this appendix we study how the impact of non-Gaussian errors on the S/N for the lensing measurement depends on shot noise, multipole range, source redshift and cosmological parameters.

The shot noise of intrinsic ellipticities contributes only to the diagonal terms of the power spectrum covariances. Hence switching off the shot noise terms in the covariances, corresponding to the case of an infinite number density of source galaxies, enhances the effect of non-Gaussian errors on the S/N , which is studied in the left panel of Figure C1. Note that, in this case, the S/N value for the Gaussian error case scales with l_{\max} as $S/N \propto l_{\max}$. Compared to Figure 3, the S/N values are significantly boosted, e.g. by an order of magnitude on $l_{\max} \gtrsim 10^4$ for the Gaussian error case. Comparing the lower panels of this plot and Figure 3 also manifests that non-Gaussian errors more degrades the S/N when the shot noise is ignored. Hence, the shot noise is found to not only significantly reduce the total S/N at $l_{\max} \gtrsim 1000$, but also mitigate the impact of the non-Gaussian errors.

The middle pane shows similar results to Figure 4, but for different choices of l_{\max} : $l_{\max} = 1000, 3000$ and 10^4 , respectively. The impact of the non-Gaussian errors appears to be very similar for these l_{\max} .

The lensing signals as well as the non-Gaussian errors are both sensitive to strengths of nonlinear mass clustering that is characterized

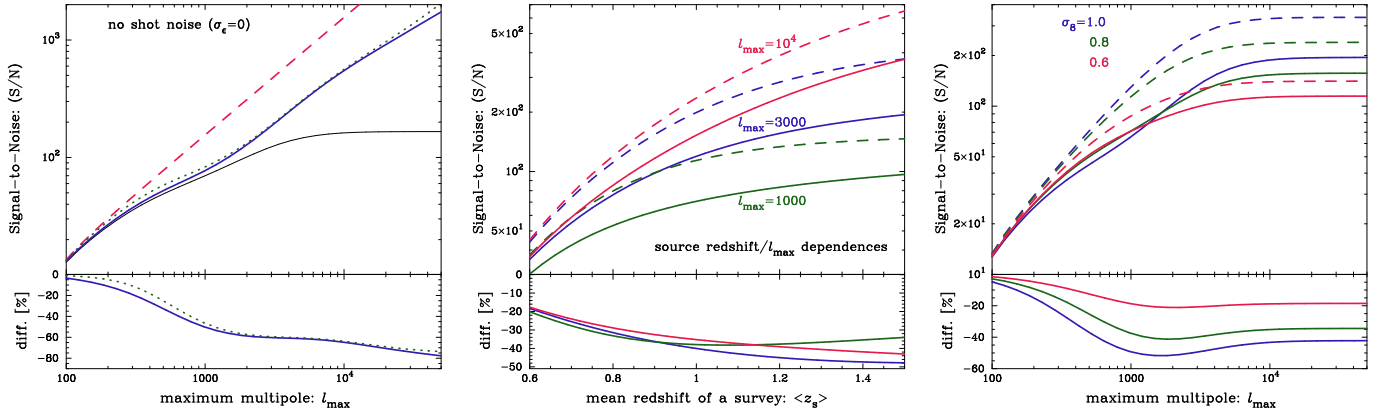


Figure C1. *Left panel:* As in Figure 3, but the shot noise due to the intrinsic ellipticities is ignored. For reference, the thin-solid curve shows the result shown by the bold-solid curve in Figure 3. Note that the y -axis range in the middle and right panels are different from those in the left panel. *Middle panel:* As in the left panel of Fig. 4, but for three different choices of the maximum multipole, $l_{\max} = 1000, 3000$ and 10^4 . The dashed and solid curves for each case of l_{\max} show the results for Gaussian and non-Gaussian errors, respectively. *Right panel:* The dependence of the total S/N on σ_8 is shown. The S/N increases with increasing σ_8 for $l_{\max} \gtrsim 2000$, but the non-Gaussian errors degrade the S/N more strongly, due to stronger nonlinear clustering.

by σ_8 . The right panel of Figure C1 shows how the S/N varies with σ_8 assumed, but other parameters being fixed. Note that our fiducial model has $\sigma_8 \simeq 0.8$. For the Gaussian error cases, the S/N amplitudes increase with increasing σ_8 as expected, due to the reduced shot noise in relative to the enhanced lensing signals. For the non-Gaussian error cases, however, the S/N amplitudes are more degraded with increasing σ_8 due to stronger nonlinearities of mass clustering, as explicitly demonstrated in the lower panel. An even more interesting is, over a range of multipoles $200 \lesssim l_{\max} \lesssim 1000$, the total S/N amplitudes decrease with σ_8 due to stronger effects of the non-Gaussian errors. Thus this modestly large dependence of the non-Gaussian covariances on σ_8 would need to be realized, if the covariances are calibrated based on simulations assuming some σ_8 that is different from the true cosmology. For example, Semboloni et al. (2007) studied the non-Gaussian covariances for the real-space cosmic shear correlation function using simulations with $\sigma_8 = 1$, so the non-Gaussian effect may be overestimated if the universe has a smaller σ_8 such as $\sigma_8 \approx 0.8$.

REFERENCES

- Albrecht, A., et al., 2006, astro-ph/0609591
 Amara, A., Refregier, A., 2007, arXiv:0710.5171
 Bartelmann, M., Schneider, P., 2001, Phys. Rep., 340, 291
 Bernardeau, F., Colombi, S., Gaztañaga, E., Scoccimarro, R., 2002, Phys. Rep., 367, 1
 Bernstein, G. M., arXiv:0808.3400
 Bernstein, G. M., Jain, B., 2004, ApJ, 600, 17
 Cooray, A., Hu, W., 2001, ApJ, 554, 56
 Cooray, A., Sheth, R., 2002, Phys. Rept., 327, 1
 Dodelson, S., *Modern Cosmology*, Academic Press, San Diego (2003).
 Eisenstein, D. J., Hu, W., 1999, ApJ, 511, 5
 Eisenstein, D. J., Hu, W., Tegmark, M., 1998, ApJ, 518, 2
 Fosalba, P., Pan, J., Szapudi, I., 2005, ApJ, 632, 29
 Fu, L., et al., arXiv:0712.0884
 Hamilton, A. J. S., Rimes, C. D., Scoccimarro, R., 2006, MNRAS, 371, 1188
 Heavens, A. F., 2003, MNRAS, 343, 1327
 Hoekstra, H., Jain, B., arXiv:0805.0139
 Hu, W., 1999, ApJ, 522, L21
 Hu, W., 2000, Phys. Rev. D, 62, 3007
 Huterer, D., 2002, Phys. Rev. D., 65, 063001
 Huterer, D., Takada, M., 2005, Astropart. Phys., 23, 369
 Huterer, D., Takada, M., Bernstein, G., Jain, B., 2006, MNRAS, 366, 101
 Ichiki, K., Takada, M., Takahashi, T., to be submitted soon.
 Jain, B., Bertschinger, E., 1994, ApJ, 431, 486
 Joachimi, B., Schneider, P., Eifler, T., 2008, A&A, 477, 43
 Komatsu, E., et al., arXiv:0803.0547
 Lee, J., Pen, U.-L., 2008, ApJ, 686, L1
 Lewis, A., Challinor, A., Lasenby, A., 2000, ApJ, 538, 473
 Limber, D. N., 1954, ApJ, 119, L655
 Ma, Z., 2007, ApJ, 665, 887
 Ma, Z., Hu, W., Huterer, D., 2005, ApJ, 636, 21

- Ma, C.-P., Fry, J. N., 2000, ApJ, 543, 503
Makino, N., Sasaki, M., Suto, Y., 1992, Phys. Rev. D, 46, 585
Massey, R., et al., 2007, MNRAS, 376, 13
Mellier, Y., 1999, ARAA, 37, 127
Miyazaki, S., et al. 2006 SPIE 6269, 9
Neyrinck, M. C., Szapudi, I., Rimes, C. D., 2006, MNRAS, 370, L66
Peacock, J. A., Smith, R. E., 2000, MNRAS, 318, 1144
Perlmutter, S., et al., 1999, ApJ, 517, 565
Riess, A. G., et al., 1998, AJ, 116, 1009
Rimes, C. D., Hamilton, A. J. S., 2005, MNRAS, 360, L82
Saito, S., Takada, M., Taruya, A., 2008, Phys. Rev. Lett., 100, 191301
Schneider, P., *Gravitational Lensing: Strong, Weak and Micro*, Lecture Notes of 33rd Saas-Fee Advanced Course, G. Meylan, P. Jetzer & P. North (eds.), Springer-Verlag: Berlin (2006).
Schneider, P., Van Waerbeke, L., Kilbinger, M., Mellier, Y., 2002, A&A, 396, 1
Scoccimarro, R., Zaldarriaga, M., Hui, L., 1999, ApJ, 527, 1
Scoccimarro, R., Sheth, R., Hui, L., Jain, B., 2001, ApJ, 546, 20
Sefusatti, E., Crocce, M., Pueblas, S., Scoccimarro, R., 2006, Phys. Rev. D, 74, 023522
Seljak, U., 2000, MNRAS, 318, 203
Seljak, U., Zaldarriaga, M., 1996, ApJ, 469, 437
Semboloni, E., Van Waerbeke, L., Heymans, C., Hamana, T., Colombi, S., White, M., Mellier, Y., 2007, MNRAS, 375, L6
Smith, R. E., et al., 2003, MNRAS, 341, 1311
Song, Y.-S., Knox, L., 2004, Phys. Rev. D, 70, 3510
Takada, M., 2006, Phys. Rev. D, 74, 043505
Takada, M., Bridle, S., 2007, New J. Phys., 9, 446
Takada, M., Jain, B., 2002, MNRAS, 337, 875
Takada, M., Jain, B., 2003a, MNRAS, 340, 580
Takada, M., Jain, B., 2003b, MNRAS, 346, 949
Takada, M., Jain, B., 2004, MNRAS, 348, 897
Takada, M., White, M., 2004, ApJ, 601, L1
Takada, M., Komatsu, E., Futamase, T., 2006, Phys. Rev. D, 73, 083520
Tegmark, M., Taylor, A. N., Heavens, A. F., 1997, ApJ, 480, 22
Tegmark, M., Hamilton, A. S. J., Xu, Y., 2002, MNRAS, 335, 887
White, M., Hu, W., 2000, ApJ, 537, 1